

HUBBLE SPACE TELESCOPE NEAR-ULTRAVIOLET SPECTROSCOPY OF BRIGHT CEMP-S STARS¹

VINICIUS M. PLACCO^{2,3}, TIMOTHY C. BEERS^{2,3}, INESE I. IVANS⁴, DAN FILLER⁴, JULIE A. IMIG⁴,
IAN U. ROEDERER^{5,3}, CARLO ABATE⁶, TERESE HANSEN⁷, JOHN J. COWAN⁸, ANNA FREBEL⁹,
JAMES E. LAWLER¹⁰, HENDRIK SCHATZ^{11,3}, CHRISTOPHER SNEDEN¹², JENNIFER S. SOBECK¹³,
WAKO AOKI¹⁴, VERNE V. SMITH¹⁵, MICHAEL BOLTE¹⁶

Draft version August 25, 2015

ABSTRACT

We present an elemental-abundance analysis, in the near-ultraviolet (NUV) spectral range, for the bright carbon-enhanced metal-poor (CEMP) stars HD 196944 ($V = 8.40$, $[\text{Fe}/\text{H}] = -2.41$) and HD 201626 ($V = 8.16$, $[\text{Fe}/\text{H}] = -1.51$), based on data acquired with the Space Telescope Imaging Spectrograph (STIS) on the *Hubble Space Telescope*. Both of these stars belong to the sub-class CEMP-*s*, and exhibit clear over-abundances of heavy elements associated with production by the slow neutron-capture process. HD 196944 has been well-studied in the optical region, but we add abundance results for six species (Ge, Nb, Mo, Lu, Pt, and Au) that are only accessible in the NUV. In addition, we provide the first determination of its orbital period, $P=1325$ days. HD 201626 has only a limited number of abundance results based on previous optical work – here we add five new species from the NUV, including Pb. We compare these results with models of binary-system evolution and *s*-process element production in stars on the asymptotic giant branch, with the goal of explaining their origin and evolution. Our best-fitting models for HD 196944 ($M_{1,i} = 0.9M_{\odot}$, $M_{2,i} = 0.86M_{\odot}$, for $[\text{Fe}/\text{H}]=-2.2$), and HD 201626 ($M_{1,i} = 0.9M_{\odot}$, $M_{2,i} = 0.76M_{\odot}$, for $[\text{Fe}/\text{H}]=-2.2$; $M_{1,i} = 1.6M_{\odot}$, $M_{2,i} = 0.59M_{\odot}$, for $[\text{Fe}/\text{H}]=-1.5$) are consistent with the current accepted scenario for the formation of CEMP-*s* stars.

Keywords: Galaxy: halo—techniques: spectroscopy—stars: abundances—stars: atmospheres—stars: Population II—stars: individual (HD 196944)—stars: individual (HD 201626)

1. INTRODUCTION

Carbon-enhanced metal-poor (CEMP) stars have received increased attention in the recent literature due to their clear importance as probes of a number of astrophysical phenomena, e.g., the production of elements by the first generations of stars in the universe (Beers & Christlieb 2005; Frebel & Norris 2015, and references therein), the mass-transfer process in binary systems (Abate et al. 2013; Abate et al. 2015a,b,c), and the nature of neutron-capture processes responsible for the production of elements beyond the iron peak (Bisterzo et al. 2010, 2011, 2012). The CEMP class of stars comprises a number of sub-classes (originally defined by Beers & Christlieb 2005, but modified somewhat by subsequent authors), based on the abundances of their neutron-capture elements: (1) CEMP-no stars, which exhibit no over-abundances of neutron-capture elements, (2) CEMP-*s* stars, which exhibit neutron-capture over-abundances consistent with the slow neutron-capture process, (3) CEMP-*r* stars, with neutron-capture over-abundances associated with the rapid neutron-capture process, and (4) CEMP-*r/s* stars, which exhibit neutron-capture over-abundances that suggest contribution from both the slow and rapid neutron-capture processes.

The great majority of abundance studies for CEMP stars have been restricted to the optical region, because samples of C-enhanced stars that are sufficiently bright to be observed at high spectral resolution in the near-ultraviolet (NUV) from space are extremely limited. Sne-

¹ The data presented herein were obtained with the (i) NASA/ESA Hubble Space Telescope, obtained at the Space Telescope Science Institute, which is operated by the Association of Universities for Research in Astronomy, Inc., under NASA contract NAS 5-26555. (These observations are associated with program GO-12554, datasets OBQ601010-30 and OBQ602010-30.); and (ii) W. M. Keck Observatory, which is operated as a scientific partnership among the California Institute of Technology, the University of California and the National Aeronautics and Space Administration. (The Observatory was made possible by the generous financial support of the W. M. Keck Foundation).

² Department of Physics, University of Notre Dame, Notre Dame, IN 46556, USA

³ JINA Center for the Evolution of the Elements, USA

⁴ Department of Physics and Astronomy, The University of Utah, Salt Lake City, UT 84112, USA

⁵ Department of Astronomy, University of Michigan, Ann Arbor, MI 48109, USA

⁶ Argelander Institut für Astronomie, Auf dem Hügel 71, 53121, Bonn, Germany

⁷ Landessternwarte, ZAH, Königstuhl 12, 69117 Heidelberg, Germany

⁸ Homer L. Dodge Department of Physics and Astronomy, University of Oklahoma, Norman, OK 73019, USA

⁹ Kavli Institute for Astrophysics and Space Research and Department of Physics, Massachusetts Institute of Technology, Cambridge, MA 02139, USA

¹⁰ Department of Physics, University of Wisconsin, Madison, WI 53706, USA

¹¹ National Superconducting Cyclotron Laboratory, Michigan State University, East Lansing, MI 48824, USA

¹² Department of Astronomy and McDonald Observatory, University of Texas, Austin, TX 78712, USA

¹³ Department of Astronomy, University of Virginia, Charlottesville, VA 22904, USA

¹⁴ National Astronomical Observatory of Japan, 2-21-1 Osawa, Mitaka, Tokyo 181-8588, Japan

¹⁵ National Optical Astronomy Observatory, Tucson, AZ 85719, USA

¹⁶ Department of Astronomy and Astrophysics, University of California, Santa Cruz, CA 95064, USA

den et al. (2003), Cowan et al. (2005), and Roederer et al. (2009) studied the STIS spectrum of CS 22892–052, a CEMP-*r* star. For CEMP-no stars, the first and only such study was the Placco et al. (2014b) analysis of the bright ($V = 9.1$), extremely metal-poor ($[\text{Fe}/\text{H}] = -3.8$) CEMP-no star BD+44°493. The authors showed that the abundances of the elements beryllium (Be, $Z=4$) and boron (B, $Z=5$) – thought to originate from cosmic-ray spallation reactions – are at the lowest level yet observed among all very and extremely metal-poor stars to date ($\log \epsilon(\text{Be}) < -2.3$ and $\log \epsilon(\text{B}) < -0.70$, respectively). Their derived upper limit on the abundance of lead (Pb; $Z=82$; $\log \epsilon(\text{Pb}) < -0.23$) is difficult to reconcile with *s*-process nucleosynthesis in low-mass asymptotic giant-branch (AGB) stars with the highest neutron exposures possible. Both of these results strengthen the argument that BD+44°493, and by implication other CEMP-no stars, could well be bona-fide second-generation stars, born from an interstellar medium polluted by massive first-generation stars (see also Frebel & Norris 2015, for a recent review).

In this study we continue our examination of the elemental-abundance patterns for CEMP stars, supplementing studies in the optical region with new NUV *Hubble Space Telescope* (*HST*) Space Telescope Imaging Spectrograph (STIS) spectroscopic data for the bright, very metal-poor CEMP-*s* stars HD 196944 and HD 201626. We obtain abundances or upper limits for a number of elements that are challenging or impossible to obtain from ground-based studies, but are nevertheless important for constraining detailed predictions of their production by AGB stars. These elements include: carbon (C; $Z=6$), oxygen (O; $Z=8$), titanium (Ti; $Z=22$), chromium (Cr; $Z=24$), manganese (Mn; $Z=25$), nickel (Ni; $Z=28$), germanium (Ge; $Z=32$), zirconium (Zr; $Z=40$), niobium (Nb; $Z=41$), molybdenum (Mo; $Z=42$), cadmium (Cd; $Z=48$), lutetium (Lu; $Z=71$), hafnium (Hf; $Z=72$), osmium (Os; $Z=76$), platinum (Pt; $Z=78$), gold (Au; $Z=79$), and lead (Pb; $Z = 82$). Section 2 describes our observations, data reduction, atmospheric parameter determinations, and radial-velocity variations. Section 3 describes our abundance analysis in detail, followed by a comparison with theoretical AGB models in Section 4. We present a brief discussion and our conclusions in Section 5.

2. OBSERVATIONS AND MEASUREMENTS

We studied high-resolution spectra of HD 196944 and HD 201626 from the NUV to optical wavelengths, employing data gathered with the *HST*/STIS and Keck/HIRES spectrographs. Below we provide a description of the observations, data reduction, and our model-atmosphere parameter determinations.

2.1. *HST*/STIS Spectra

STIS (Kimble et al. 1998; Woodgate et al. 1998) observations of HD 196944 and HD 201626 were obtained as part of Program GO-12554, using the E230M echelle grating, centered at 2707 Å, and the NUV Multianode Microchannel Array (MAMA) detector. There was one observational sequence of three individual exposures for each star, taken on 2012 April 29 (HD 201626) and 2012 September 22 (HD 196944). The total integration time was about 7.9 ks per star. The $0''.06 \times 0''.2$ slit yields a

resolving power of $R \sim 30,000$. Our setup produced a wavelength coverage from 2280 Å–3070 Å in a single exposure. The observations were reduced and calibrated using the standard *calstis* pipeline. The S/N of the combined spectrum varies from $\sim 45 \text{ pix}^{-1}$ near 2300 Å, to $\sim 70 \text{ pix}^{-1}$ near 2700 Å, to $>90 \text{ pix}^{-1}$ near 3070 Å.

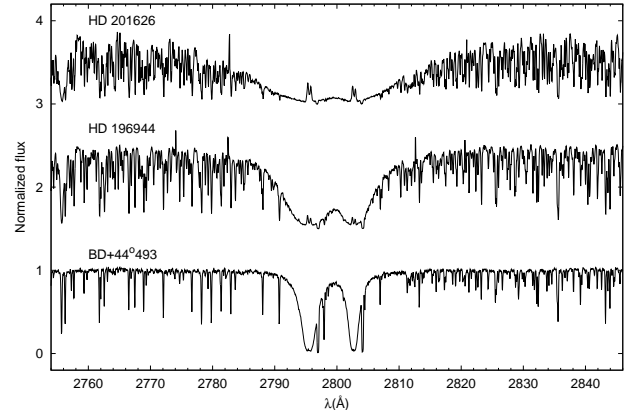


Figure 1. *HST*/STIS NUV spectra for HD 201626 ($[\text{Fe}/\text{H}] = -1.51$) and HD 196944 ($[\text{Fe}/\text{H}] = -2.41$), compared with the spectrum of the EMP BD+44°493 ($[\text{Fe}/\text{H}] = -3.80$). The region shown includes the Mg II doublet at 2800 Å. These stars have similar T_{eff} ; the differences in metallicity are apparent.

The NUV spectra of the program stars around the Mg II doublet at 2800 Å are shown in Figure 1. For comparison, *HST*/STIS spectra of the CEMP-no star BD+44°493 (obtained during this same program and analysed by Placco et al. 2014b) is also shown. The effective temperatures and surface gravities of the program stars are comparable to BD+44°493, but their metallicities are higher by 1.4–2.3 dex. To better illustrate the intrinsic differences between these CEMP-*s* stars and CEMP-no stars, Figure 2 shows portions of the NUV spectra around the lines of four neutron-capture elements for the same three stars shown in Figure 1. Note in particular the absence of absorption by Cd I, Os II, Lu II, and Pb I for BD+44°493, which signal a lack of neutron-capture enhancement in BD+44°493 relative to HD 196944 and HD 201626.

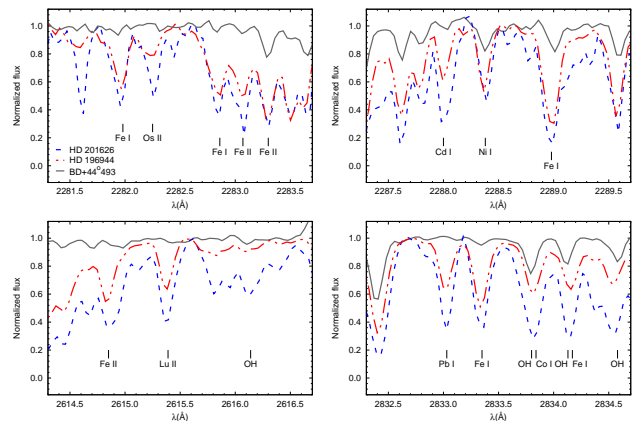


Figure 2. *HST*/STIS NUV spectra for HD 201626 and HD 196944, compared to the spectrum of BD+44°493, in the regions of the lines of Os II, Cd I, Lu II, and Pb I.

2.2. HIRES Spectra

The Keck/HIRES (Vogt et al. 1994) spectra of both stars were gathered over two observing runs: 2004 October 1 (program ID: C23H and PI: I. Ivans) and 2007 June 5 and 7 (program ID: U100Hb and PI: M. Bolte). HD 196944 was observed in three 300s integrations in both runs. HD 201626 was observed with three 450s integrations in program C23H and three 240s integrations in program U100Hb. The U100Hb data cover the wavelength range $3725 \text{ \AA} \lesssim \lambda \lesssim 7990 \text{ \AA}$, with resolution $R \equiv \lambda/\Delta\lambda = 103,000$. The C23H data cover bluer wavelengths ($2990 \text{ \AA} \lesssim \lambda \lesssim 5850 \text{ \AA}$), with resolution $R = 48,000$.

The C23H data were reduced using standard tasks in IRAF¹⁷, including bias subtraction, bad-pixel interpolation, and wavelength calibration; and in FIGARO¹⁸, including flat-fielding, light cosmic ray excision, both sky and scattered-light subtraction, and extraction of the one-dimensional spectra. The same reduction steps were performed on the U100Hb data using the MAKEE pipeline (2008 version 5.2.4)¹⁹. Final processing of the HIRES data, including continuum normalization and co-addition of the trios of extracted spectra were done using SPECTREdsg (D. S. Gregersen, priv. comm.), an updated version of the SPECTRE package (Fitzpatrick & Sneden 1987).

2.3. Atmospheric Parameters

We determined self-consistent stellar model-atmosphere parameters using spectroscopic constraints on the abundances of neutral and ionized species of the same element. For CEMP and other cool stars, equivalent-width measurements (EWs) of clean unblended iron (Fe) lines are usually employed. However, the NUV region of our stars is extremely rich and complex. Thus, we derived our atmospheric parameters using the EWs of Fe I and Fe II lines in the optical wavelength range. We then employed this model atmosphere to derive the remaining abundances at both NUV and optical wavelengths.

Our EWs were obtained using the following tools:

- (i) Fitting Gaussian profiles to the observed atomic lines, using the Robospect package (Waters & Hollek 2013).
- (ii) Fitting Gaussian and Voigt profiles, using the SPECTREdsg package, an updated version of the SPECTRE package (Fitzpatrick & Sneden 1987).
- (iii) Fitting Gaussian and Voigt profiles, using the THIMBLES package (Anderton 2015).

We compared the measurements obtained using the THIMBLES and SPECTREdsg packages. For 100 lines in common between two sets of independent measurements, the difference in reduced equivalent widths, $\text{REW} \equiv \log(\text{EW})/\lambda = 0.01 \pm 0.05$.

¹⁷ IRAF is distributed by NOAO, which is operated by AURA, under cooperative agreement with the NSF.

¹⁸ FIGARO is provided by the Starlink Project, which is run by CCLRC on behalf of PPARC (UK).

¹⁹ http://www.astro.caltech.edu/~tb/ipac_staff/tab/makee/index.html

The Robospect line lists were based on the compilation of Roederer et al. (2012), and data retrieved from the VALD database (Kupka et al. 1999) and the National Institute of Standards and Technology Atomic Spectra Database (NIST; Kramida et al. 2013). The SPECTREdsg and THIMBLES line lists are based on those used in Ivans et al. (2003, 2006), supplemented and updated by the work of Blackwell-Whitehead & Bergemann (2007), Nilsson & Ivarsson (2008), Meléndez & Barbuy (2009), Simmerer et al. (2013) Wood et al. (2013), Lawler et al. (2014), Ruffoni et al. (2014), Wood et al. (2014a,b), and Andersson et al. (2015).

The atmospheric parameters of the stellar models we employed in our analysis were derived from these HIRES spectra, employing the following spectroscopic constraints. The effective temperature (T_{eff}) was determined by minimizing any trend between the abundances of Fe I absorption lines with the excitation potential (χ); the surface gravity ($\log g$) was determined by the equilibrium balance between the abundances of Fe I and Fe II; and the microturbulent velocity (ξ) was determined by minimizing the trend between the Fe I abundances derived for the individual lines and their REWs.

For HD 196944, we derived the best stellar model-atmosphere parameters to be $5170 \pm 100 / 1.60 \pm 0.25 / -2.41 \pm 0.25 / 1.55 \pm 0.10$ [T_{eff} (K) / $\log g$ (cgs) / [Fe/H] / ξ (km s⁻¹)]. Our values are consistent with previous determinations from the literature, listed in Table 1. For HD 201626, we derived the best stellar model-atmosphere parameters to be $5175 \pm 150 / 2.80 \pm 0.45 / -1.51 \pm 0.25 / 1.30 \pm 0.10$. Despite the large literature on HD 201626, the derived stellar model-atmosphere parameters are not in very good agreement between several different authors, as seen in Table 1. The Karinkuzhi & Goswami (2014) model-atmosphere parameter estimates agree reasonably well with ours (within 50 K for T_{eff} and 0.1 dex for [Fe/H]), apart from a 0.55 dex difference in $\log g$. Both studies derived T_{eff} values from spectroscopic constraints on the abundances. However, Aoki & Tsuji (1997) adopted a T_{eff} based on the infrared flux method (Blackwell et al. 1980), and Sneden et al. (2014) adopted one based on the $V - K$ color of the star (Ramirez & Melendez 2005), albeit with a low reddening value ($E(V - K) \simeq 0.171$). Table 1 also contains additional colour-based estimates we have made of some of the stellar parameters.

To investigate the temperature estimate for HD 201626 issue further, we performed the following experiment. Using a stellar-atmosphere model with the Aoki & Tsuji (1997) parameter estimates, we find $\log \epsilon(\text{Fe I}) = 5.50$ and $\log \epsilon(\text{Fe II}) = 5.60$; with the Sneden et al. (2014) parameters, we find $\log \epsilon(\text{Fe I}) = 5.57$ and $\log \epsilon(\text{Fe II}) = 5.30$. Thus, demanding a cooler T_{eff} for this star drives the derived metallicity lower, much closer to the [Fe/H] adopted by Sneden et al. (2014). If there was an independent method of establishing the metallicity of the star other than by the spectroscopic methods we have employed in this study, a lower [Fe/H] might indicate that we have the T_{eff} wrong for HD 201626. However, the abundances derived from these other models do not satisfy the spectroscopic constraints that we employed.

While we acknowledge the tension between the spectroscopically derived T_{eff} values and those derived over a

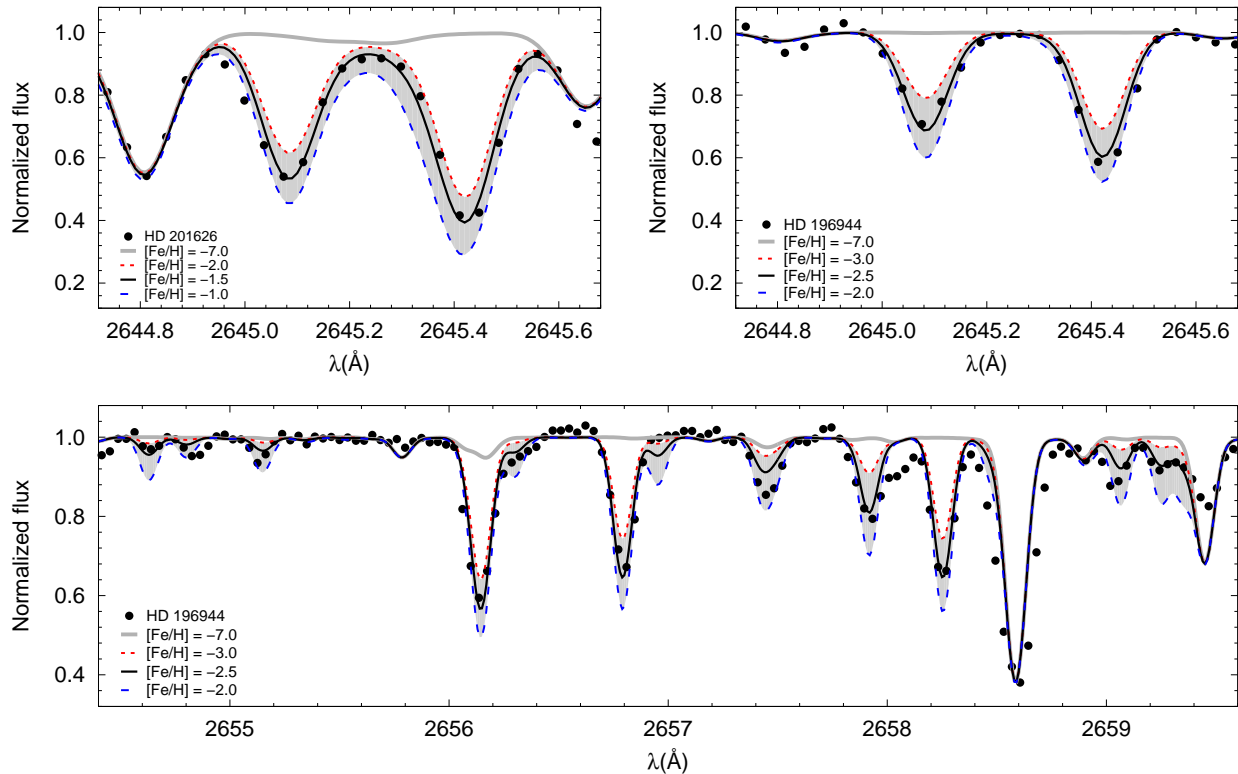


Figure 3. Spectral synthesis of NUV Fe I and Fe II features for HD 196944 and HD 201626. The dots represent the observed spectra, the solid line is the best abundance fit, and the dotted and dashed line are the lower and upper abundance limits, used to estimate the abundance uncertainty. The shaded area encompasses a 1.0 dex difference in $\log \epsilon(\text{Fe})$. The light gray line shows the synthesized spectrum in the absence of Fe.

broader wavelength range for HD 201626, the underlying cause is beyond the scope of this analysis. Our stellar model-atmosphere parameters are derived from superb high-resolution spectra; our line list is extensive (see Table 2); and, as we show in Section 3, we find excellent agreement between neutral and ionized states of multiple elements. Of greatest importance for this analysis is that our spectroscopically derived stellar model-atmosphere parameters produce spectrum-synthesis calculations that match the observed data in the NUV wavelengths.

Figure 3 shows a portion of the NUV spectra of both HD 196944 and HD 201626, in a region with a number of Fe I and Fe II features. The dots represent the observed spectra, the solid line is the best abundance fit, generated with the atmospheric parameters determined from the optical spectra. The dotted and dashed lines limit the shaded area, which encompass a 1.0 dex difference in $[\text{Fe}/\text{H}]$. As can be seen from inspection of this figure, the fit is excellent.

2.4. Radial-Velocity Variations

Heliocentric radial velocities for the program stars were determined from clean unblended lines in the optical spectra. For HD 196944, we derived $V_r = -176.40 \pm 0.60 \text{ km s}^{-1}$ on MJD 53279.255346; $V_r = -169.40 \pm 0.30 \text{ km s}^{-1}$ on MJD 54256.557629; and $V_r = -174.30 \pm 0.20 \text{ km s}^{-1}$ on MJD 54574.636680²⁰. This star has a number of V_r measurements from the literature: $V_r = -174.76 \pm 0.36 \text{ km s}^{-1}$ (Aoki et al. 2002);

$V_r = -174.10 \pm 0.40 \text{ km s}^{-1}$ (Van Eck et al. 2003); $V_r = -169.29 \pm 0.08 \text{ km s}^{-1}$ (Lucatello et al. 2005); $V_r = -168.49 \pm 0.11 \text{ km s}^{-1}$ (Lucatello et al. 2005); $V_r = -166.40 \pm 0.30 \text{ km s}^{-1}$ (Roederer et al. 2008); and $V_r = -166.80 \pm 0.70 \text{ km s}^{-1}$ (Roederer et al. 2014a). These radial-velocity variations indicate that HD 196944 is a member of a binary or multiple system. However, there is no published value of its period based on these measurements. From the values determined by this work and from the literature, we were able to estimate a period for HD 196944. We have used a program described in Buchhave et al. (2010), based on the formalism of Pál (2009), which models a Keplerian orbit to the data. Assuming initial guesses of the period and ephemeris, we were able to determine a period of 1325 ± 12 days, and an eccentricity of 0.015 ± 0.036 .

For HD 201626, we derived $V_r = -150.20 \pm 1.70 \text{ km s}^{-1}$ on MJD 53279.325761; and $V_r = -140.00 \pm 0.30 \text{ km s}^{-1}$ on MJD 54258.560998. Literature values include 26 measurements from McClure & Woodsworth (1990), and also the following: $V_r = -149.40 \pm 0.80 \text{ km s}^{-1}$ (Van Eck et al. 2003); $V_r = -145.70 \pm 0.70 \text{ km s}^{-1}$ (Nordström et al. 2004); $V_r = -141.60 \pm 1.20 \text{ km s}^{-1}$ (Karinkuzhi & Goswami 2014). HD 201626 is a confirmed binary with a period of 1465 ± 15 days, and an eccentricity of 0.103 ± 0.038 (McClure & Woodsworth 1990). From our derived radial-velocities and the values with available MJD, we were able to determine a period of 1470 ± 9 days, and an eccentricity of 0.090 ± 0.051 , which are consistent with the values from the literature.

²⁰ Keck/HIRES data gathered on 2008 April 14 (program ID: U013Hr and PI: M. Bolte), the middle of five exposures.

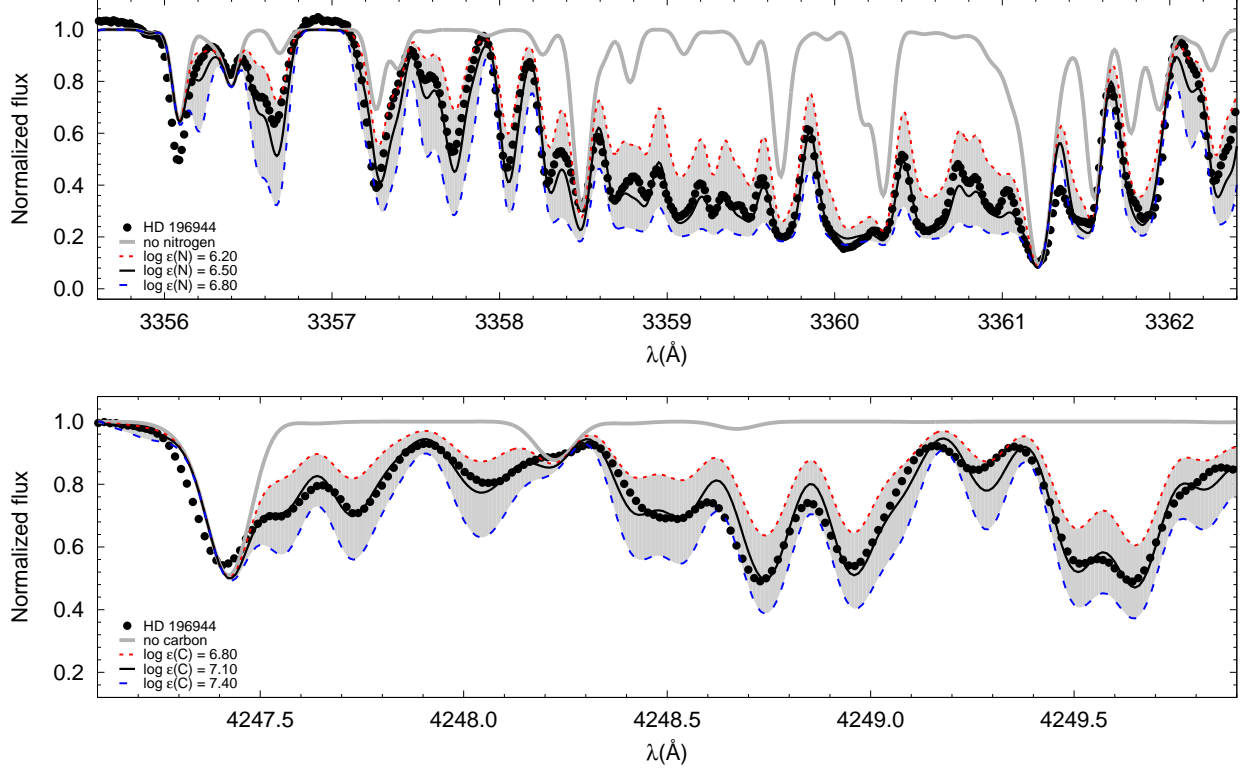


Figure 4. Spectral synthesis of the optical NH (top panel) and CH (bottom panel) features for HD 196944. The dots represent the observed spectra, the solid line is the best abundance fit, and the dotted and dashed lines are the lower and upper abundance limits, used to estimate the abundance uncertainty. The shaded area encompasses a 0.6 dex difference in $\log \epsilon(N)$ and $\log \epsilon(C)$. The light gray line shows the synthesized spectrum in the absence of N and C.

3. ELEMENTAL-ABUNDANCE ANALYSIS AND UPPER LIMITS

Elemental-abundance estimates or upper limits were obtained from the NUV and optical spectra of HD 196944 and HD 201626 for 34 elements: C, nitrogen (N; $Z=7$), O, sodium (Na; $Z=11$), magnesium (Mg; $Z=12$), silicon (Si; $Z=14$), calcium (Ca; $Z=20$), scandium (Sc; $Z=21$), Ti, vanadium (V; $Z=23$), Cr, Mn, iron (Fe; $Z=26$), cobalt (Co; $Z=27$), Ni, zinc (Zn; $Z=30$), Ge, strontium (Sr; $Z=38$), yttrium (Y; $Z=39$), Zr, Nb, Mo, Cd, barium (Ba; $Z=56$), lanthanum (La; $Z=57$), cerium (Ce; $Z=58$), neodymium (Nd; $Z=60$), europium (Eu; $Z=63$), Lu, Hf, Os, Pt, Au, and Pb.

Our spectral analysis utilizes the grid of one-dimensional plane-parallel ATLAS9 model atmospheres with no overshooting and improved opacity distribution functions (Castelli & Kurucz 2004), computed under the assumption of local thermodynamic equilibrium (LTE)²¹. We use the 2011 version of the MOOG synthesis code (Snedden 1973) for this analysis. To treat isotropic coherent scattering in this version of MOOG, the solution of the radiative transfer considers both absorption and scattering components, rather than treating such scattering as pure absorption (see Sobek et al. 2011, for further details).

Our final abundance ratios, $[X/Fe]$, are given with respect to the solar abundances of Asplund et al. (2009). Abundances and upper limits for lines derived from both EWs and spectral synthesis are listed in Table 2 (opti-

cal) and Table 3 (NUV). The average chemical abundances and upper limits for HD 196944 and HD 201626 are listed in Table 4 (optical) and Table 5 (NUV). The σ value refers to the standard error of the mean. We also evaluated the effect of changes in each atmospheric parameter on the determined abundances. For this purpose we used spectral lines with abundances determined by equivalent-width analysis. The adopted variations are 150 K for T_{eff} , 0.5 dex for $\log g$, and 0.3 km s^{-1} for v_{micro} . Results are shown in Table 6. Also shown is the total uncertainty, σ_{tot} , which is calculated from the quadratic sum of the individual errors.

3.1. Carbon, Nitrogen, and Oxygen

Carbon, nitrogen, and oxygen abundances were determined for both stars, using the NUV and optical spectra, from both EW analyses and spectral synthesis calculations.

Carbon abundances were determined from optical CH features at 4246 Å and 4313 Å. For HD 196944, both regions are consistent with $\log \epsilon(C)=7.10$ and, for HD 201626, $\log \epsilon(C)=8.40$. The lower panels of Figures 4 and 5 show the synthesis for the 4246 Å region in both stars. We derived an isotopic ratio $^{12}\text{C}/^{13}\text{C} = 4$ for HD 196944, and $^{12}\text{C}/^{13}\text{C} = 50$ for HD 201626. The high $^{12}\text{C}/^{13}\text{C}$ for HD 201626 is consistent with AGB models, and the low value for HD 196944 can be explained by its evolutionary stage, in which internal mixing slightly decreased the $^{12}\text{C}/^{13}\text{C}$ ratio. We also attempted to determine the carbon abundance from the C I atomic features at 2478 Å and 2967 Å. For HD 196944,

²¹ <http://kurucz.harvard.edu/grids.html>

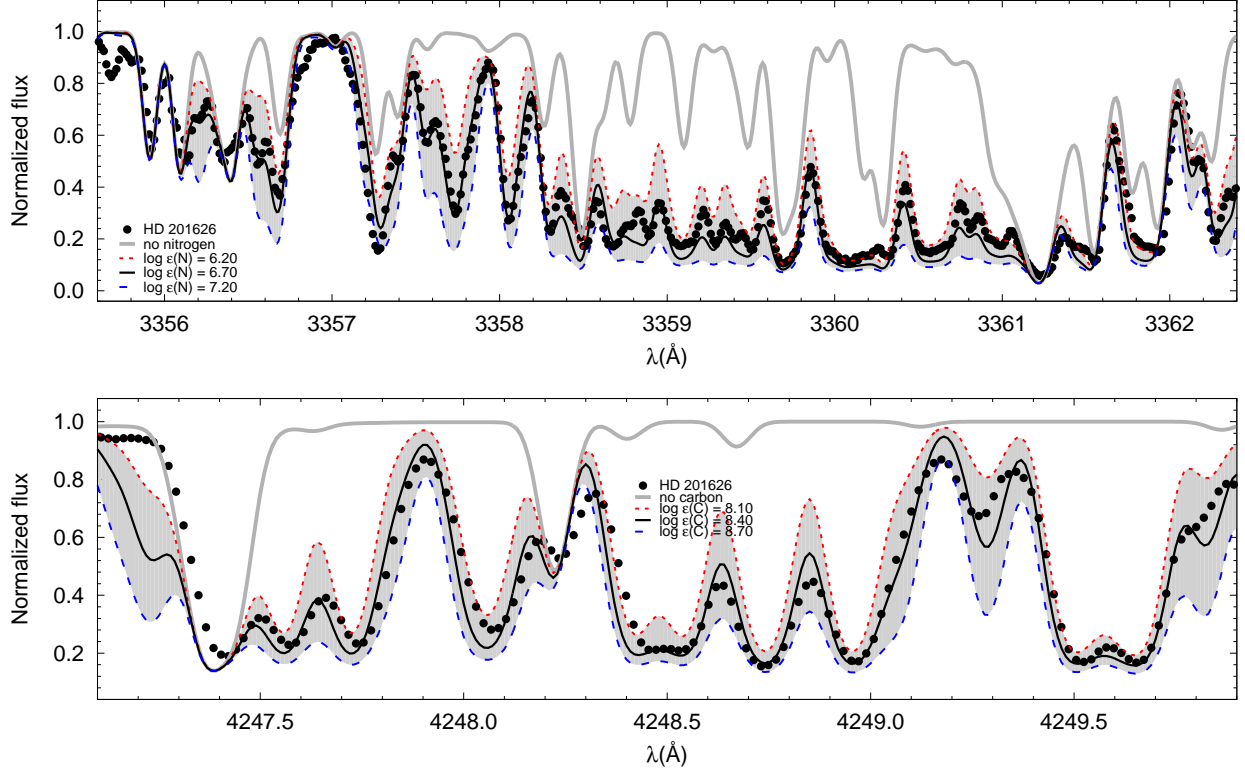


Figure 5. Spectral synthesis of the optical NH (top panel) and CH (bottom panel) features for HD 201626. The dots represent the observed spectra, the solid line is the best abundance fit, and the dotted and dashed line are the lower and upper abundance limits, used to estimate the abundance uncertainty. The shaded area encompasses a 1.0 dex difference in $\log \epsilon(\text{N})$ and 0.6 dex in $\log \epsilon(\text{C})$. The light gray line shows the synthesized spectrum in the absence of N and C.

the $\log \epsilon(\text{C})=7.10$ value determined for the optical spectra can be well-reproduced for the 2478 Å line (upper panel of Figure 6). The agreement between abundances determined from the atomic (NUV) and molecular (optical) features is worth noting, since previous works (Asplund 2005; Collet et al. 2007) have suggested that 3D effects on the CH and C₂ bands could lead to overestimates of [C/Fe] of +0.5 to +0.8 dex in metal-poor subgiants. For HD 201626, both regions are heavily blended with other species, and it was not possible to determine abundances. We also calculated the carbon-abundance corrections for both stars, based on the procedure described by Placco et al. (2014a). This procedure takes into account the evolutionary status of the star (from the $\log g$ value) to find a correction for the carbon depletion, which occurs during stellar evolution on the giant branch. Since HD 196944 is a red horizontal-branch star, we take its carbon correction only as a lower limit. Using the [N/Fe]=0.0 case, we find corrections of $> +0.23$ dex for HD 196944, and 0.02 dex for HD 201626.

Nitrogen abundances were determined from the NH feature at 3360 Å. The line list was provided by Kurucz (1993), following the procedure described in Aoki et al. (2006). For HD 196944, the best value is $\log \epsilon(\text{N})=6.50$ (upper panel of Figure 4) and, for HD 201626, $\log \epsilon(\text{N})=6.70$ (upper panel of Figure 5).

Oxygen abundances were determined from NUV spectral synthesis of OH features for HD 196944, and spectrum synthesis of the [O I] 6301 Å line for HD 201626. For HD 201626, we were also able to measure the O triplet near 7700 Å. However, we do not include the abun-

dances from these lines in our analysis, for reasons we describe below.

The O-triplet features possess high excitation potentials, and are expected to suffer from non-LTE effects. For HD 201626, LTE analysis of the O-triplet EWs yields $\log \epsilon(\text{O})=8.15$, with a standard deviation of 0.17 dex (based on the line-to-line scatter). Applying the recommended correction of Takeda (2003) for each of the three lines, we derive $\log \epsilon(\text{O})=8.05$, which is closer to that of the abundance we derive from spectrum-synthesis calculations of the [O I] 6301 Å feature. A star with atmospheric parameters close to those of HD 201626 was studied by Garcia Perez et al. (2006) (HD 274949: 5090/2.76/−1.51), who independently calculated non-LTE abundance corrections for the triplet. Their $\Delta \log \epsilon(\text{O})$ correction is −0.10 dex, in agreement with the value we find adopting the recommended correction of Takeda (2003). However, in a comparison against Takeda (2003), Fabbian et al. (2009) find the necessary non-LTE corrections to be significantly larger than those reported by Takeda (2003) for stars warmer than 5500 K. Fabbian et al. (2009) also note that the stellar metallicity plays an important role in the degree of the non-LTE effect. For the stars included in the study of Ramirez et al. (2013) that are closest in their stellar parameters to HD 201626 (HIP 60719: 5250/2.7/−2.42 and HIP 18235: 5010/3.2/−0.73) the corrections to the LTE $\log \epsilon(\text{O})$ abundance derived from the triplet are $\Delta \log \epsilon(\text{O})$ of +0.66 dex and −0.29 dex, an order of magnitude difference. Thus, in our analysis of HD 201626, we rely on the abundance derived from the [O I] 6301 Å

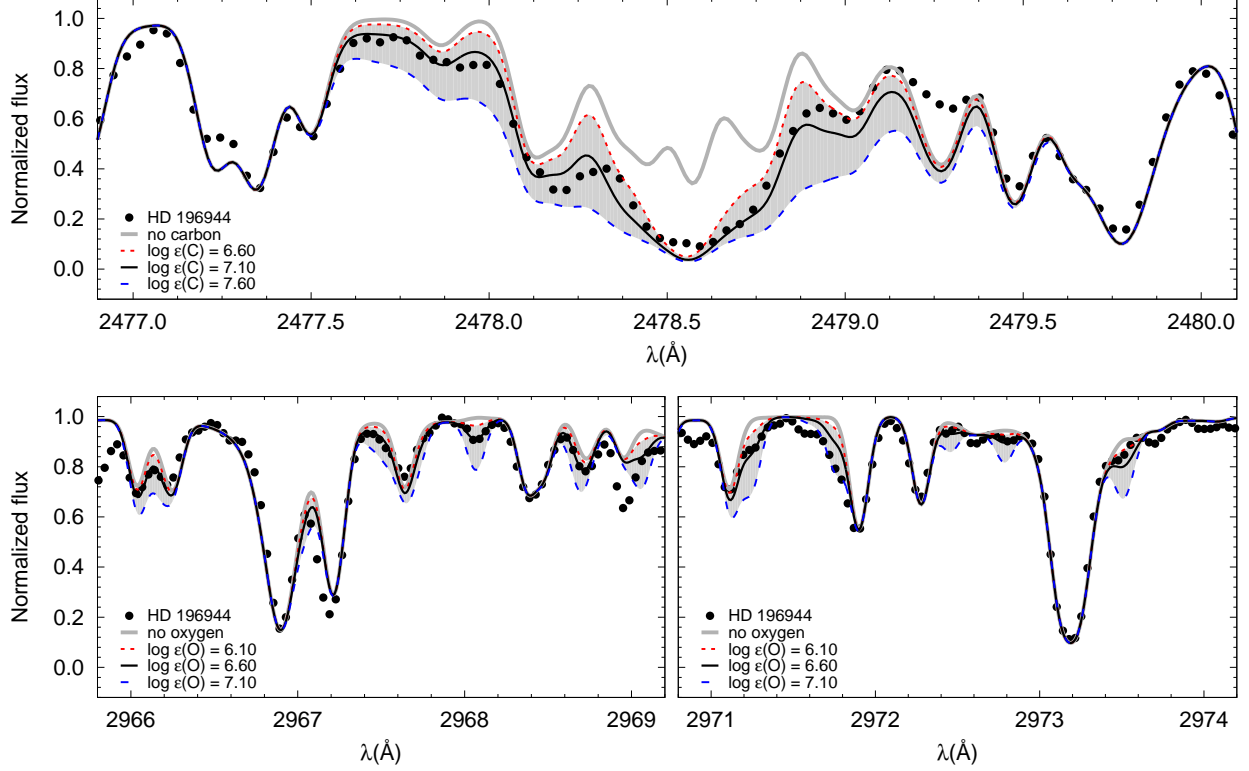


Figure 6. Spectral synthesis of the NUV C I (top panel) and OH (bottom panel) features for HD 196944. The dots represent the observed spectra, the solid line is the best abundance fit, and the dotted and dashed line are the lower and upper abundance limits, used to estimate the abundance uncertainty. The shaded area encompasses a 1.0 dex difference in $\log \epsilon(\text{C})$ and $\log \epsilon(\text{O})$. The light gray line shows the synthesized spectrum in the absence of C and O.

line.

There are several OH features in the 2965–2975 Å region of HD 196944 (lower panels of Figure 6). These were all be reasonably fit with a $\log \epsilon(\text{O})=6.60$. However, we conservatively adopt a 0.3 dex uncertainty, due to the presence of a few unknown features in this region.

3.2. The Iron-Peak Elements

Abundances for Ti, Cr, and Ni from the NUV spectra were determined for HD 196944 with an EW analysis. No such measurements were made for HD 201626, since it is more metal-rich and the same NUV lines are heavily blended. We derived Mn II abundances from spectral synthesis of NUV features at 2933 Å and 2949 Å for both stars, because these lines are broadened by hyperfine splitting of the ^{55}Mn isotope. Figure 7 (upper panels) shows the synthesis of the 2933 Å Mn II line in the NUV spectrum for both program stars. We were also able to determine the abundance of Ge in both stars. This element belongs to the transition between iron-group and neutron-capture elements. Three lines (2651 Å, 2691 Å, and 3039 Å) were measured for HD 196944, and one line (2691 Å) for HD 201626. The lower panels of Figure 7 show the spectral synthesis for the Ge I 2691 Å line.

A number of iron-peak element abundances were determined from EW analysis of the optical spectra of HD 196944 and HD 201626. Comparing the optical and NUV determinations, we find good agreement for Ti, Cr, and Ni for HD 196944, and Mn for both stars. For elements with two different ionization states measured

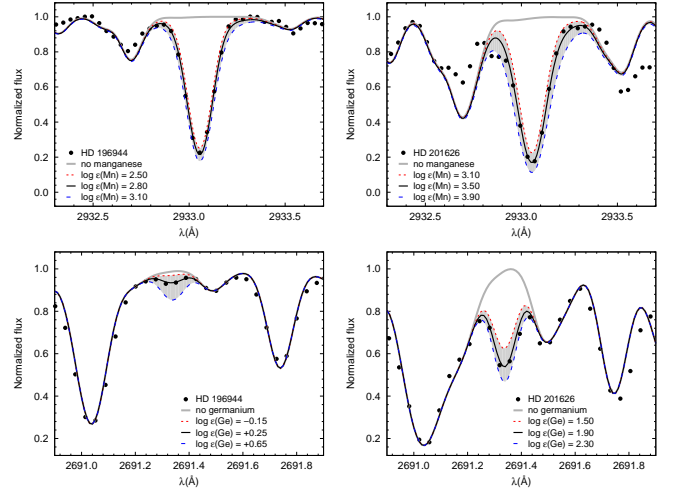


Figure 7. Spectral synthesis of the NUV Mn II and Ge I features for HD 196944 and HD 201626. The dots represent the observed spectra, the solid line is the best abundance fit, and the dotted and dashed line are the lower and upper abundance limits, used to estimate the abundance uncertainty. The shaded area encompasses a 0.6–0.8 dex difference in $\log \epsilon(\text{Mn})$ and $\log \epsilon(\text{Ge})$. The light gray line shows the synthesized spectrum in the absence of Mn and Ge.

in HD 196944, abundances are within 0.04 dex for Ti and 0.22 dex for Cr obtained from the optical data, and 0.02 dex for Ti, 0.18 dex for Cr, and 0.40 dex for Ni from the NUV data. The good agreement between the Ti I and Ti II also confirms our spectroscopically determined $\log g$ values. The large difference for Ni lines in the NUV is mainly due to the difficulty of measuring EWs for the

Ni II lines.

3.3. The Neutron-Capture Elements

For the neutron-capture elements (Cu to Pb), all of the abundances listed in Tables 4 and 5 were determined from spectrum-synthesis calculations, using both optical and NUV spectra. For the optical spectra, some elements had their abundances first estimated from their EW that were used as starting points for the synthesis.

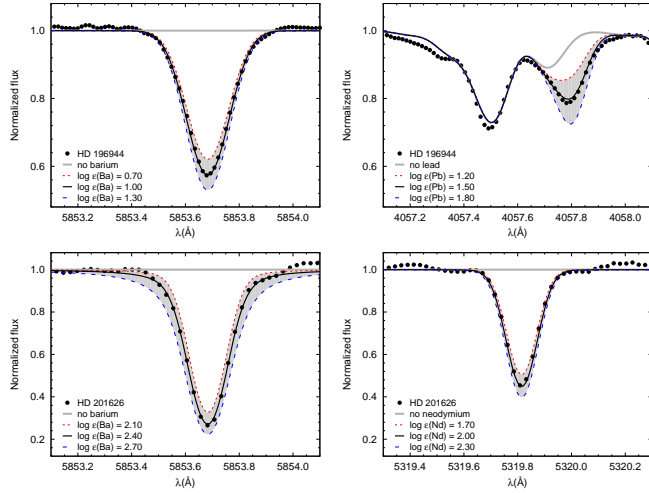


Figure 8. Spectral synthesis of the optical Ba II, Nd II, and Pb I features for HD 196944 and HD 201626. The dots represent the observed spectra, the solid line is the best abundance fit, and the dotted and dashed line are the lower and upper abundance limits, used to estimate the abundance uncertainty. The shaded area encompasses a 0.6 dex difference in the abundances. The light gray line shows the synthesized spectrum in the absence of the listed species.

There are a number of unblended Zr II lines in the NUV region of the spectra of these stars. For both HD 196944 and HD 201626, the agreement between the individual abundances is generally good (between 0.1–0.2 dex), apart from the 2699 Å feature, which is consistently lower by about 0.5 dex. Ba II lines are broadened by hyperfine splitting (hfs) of the ^{135}Ba and ^{137}Ba isotopes; so even though we also determined Ba abundances from EW analysis, the final average values come from spectral synthesis only. Figure 8 shows the optical spectral synthesis of the Ba II 5853 Å line for both stars, the Pb I 4057 Å line for HD 196944, and the Nd II 5319 Å line for HD 201626. The EW Ba abundances for HD 196944 agree within 0.1 dex with the spectral synthesis for the 4554 Å, 5853 Å, and 6141 Å lines ($\log \epsilon(\text{Ba})=1.0$). For HD 201626, we report the abundance from the spectrum synthesis of the 5853 Å feature. The synthesis of the 6141 Å and 6406 Å features are consistent with this value, but the 4554 Å region is too complex to model well²².

Figure 9 shows the spectral synthesis of Lu, Hf, Au, and Nb for HD 196944, and Pb (2833 Å line) for both stars. Pb abundances determined from neutral species are more affected by non-LTE effects than abundances

determined from ionized species. For the stellar parameters of the stars studied in this work, this effect can increase the Pb abundance by up to 0.5 dex (Mashonkina et al. 2012). This effect is somewhat counterbalanced by considering 3D modeling (Siqueira Mello et al. 2013). For simplicity, we consider the combination of both effects to be within the uncertainties of the spectral synthesis. Overall, we were able to reproduce the observed spectra with our line list, even with difficult blends, such as the one for the Au I 2675 Å line. For HD 196944, there is a small discrepancy between the Pb abundances determined from the 2833 Å ($\log \epsilon(\text{Pb})=1.35$) and 4057 Å ($\log \epsilon(\text{Pb})=1.50$) lines.

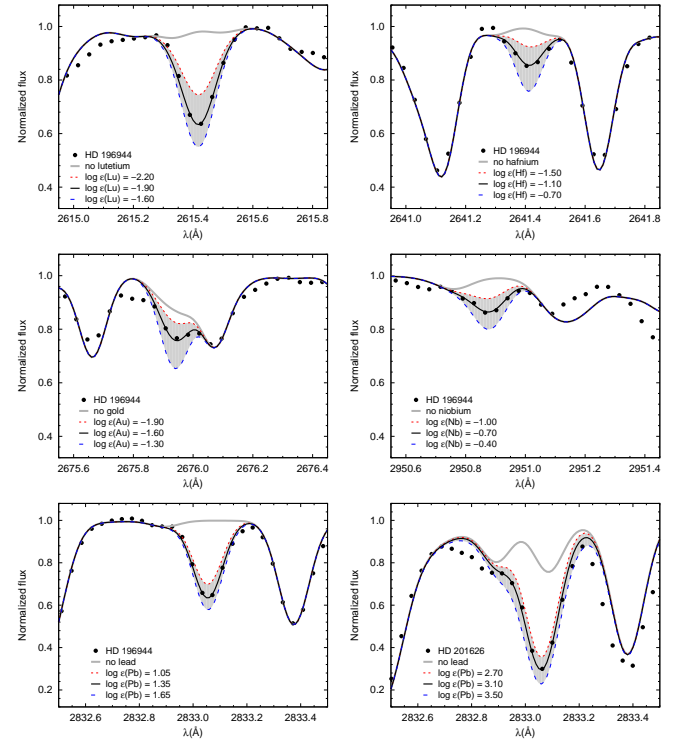


Figure 9. Spectral synthesis of the NUV Lu II, Hf II, Au I, and Nb I features for HD 196944, and Pb I for both stars. The dots represent the observed spectra, the solid line is the best abundance fit, and the dotted and dashed line are the lower and upper abundance limits, used to estimate the abundance uncertainty. The shaded area encompasses a 0.6–0.8 dex difference in the abundances. The light gray line shows the synthesized spectrum in the absence of the listed species.

4. DISCUSSION

The general behavior of the elemental-abundance patterns for CEMP-*s* stars is understood and well-explained by the evolution in a binary system with a more massive companion going through the AGB phase and polluting the atmosphere of the currently observed, less massive star. However, there is still debate on the range of masses of the AGB donor star, as well as the details of the mass transfer, dilution effects, and orbital features of the binary system. Elemental and isotopic abundances for CEMP-*s* stars can help distinguish between different models. For HD 196944 and HD 201626, we evaluated the chemical abundance patterns by comparing their optical and NUV determinations with AGB yields from Bis-

²² Using the $T_{\text{eff}}=4800$ K models, spectrum-synthesis calculations of molecule-rich regions showed no improvement over the syntheses produced employing the model derived in this study.

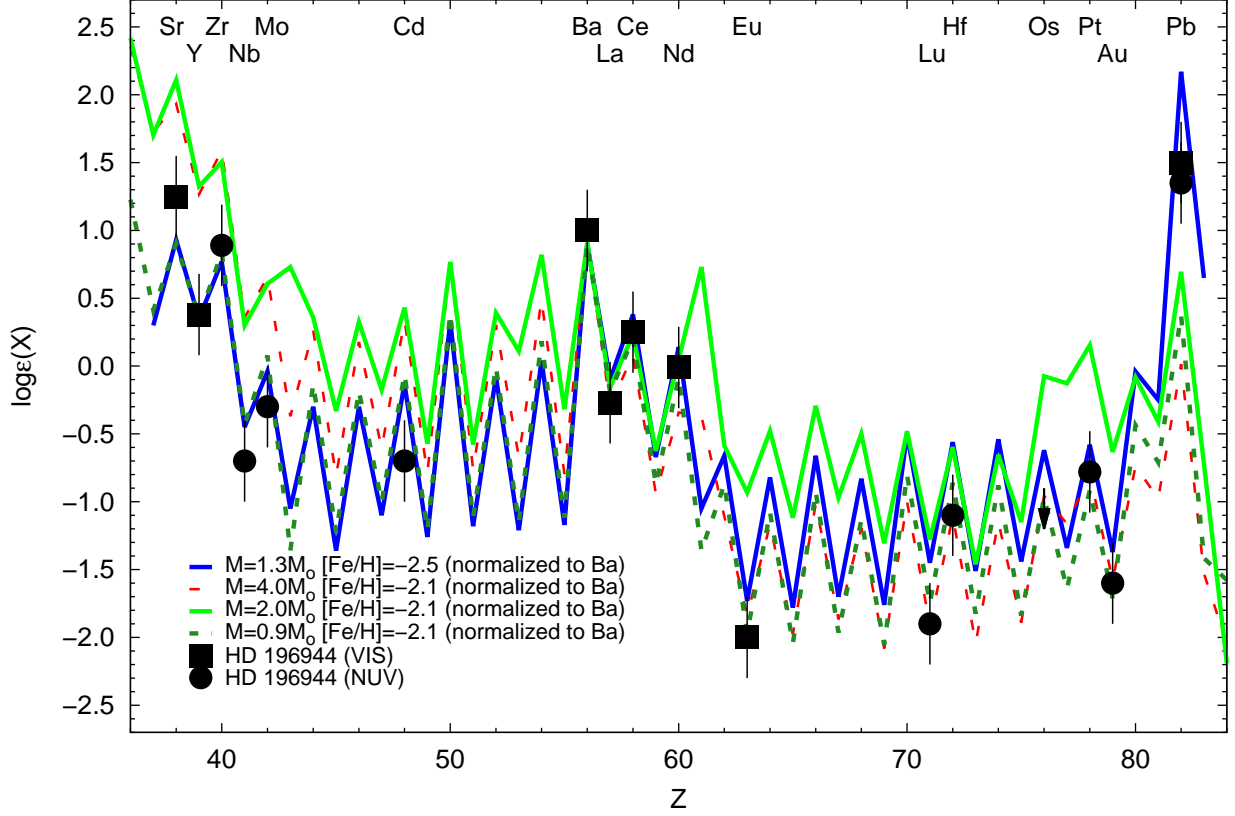


Figure 10. Comparison between elemental-abundances and upper limits determined from this work for HD 196944, and theoretical yields for four different AGB models from Bisterzo et al. (2011) and Placco et al. (2013). The models are normalized to the optical Ba abundance estimate.

terzo et al. (2010) and Placco et al. (2013), as well as a model of binary evolution and AGB nucleosynthesis from Abate et al. (2015a).

4.1. Comparison with Bisterzo et al. (2010)

Figure 10 shows the optical and NUV abundances for HD 196944, compared with AGB yields from the model presented in Placco et al. (2013), with $M = 1.3 M_{\odot}$ and $[\text{Fe}/\text{H}] = -2.5$, as well as three additional models from Bisterzo et al. (2010), with $[\text{Fe}/\text{H}] = -2.1$ and $M = 0.9, 2.0$, and $4.0 M_{\odot}$. Although all the models well-reproduce the second peak of the *s*-process (Ba-Nd), the more massive AGB stars over-produce the first-peak *s*-process elements (Sr, Y, and Zr). In addition, Pb is under-produced by the $[\text{Fe}/\text{H}] = -2.1$ models, and the observed values are closer to the $[\text{Fe}/\text{H}] = -2.5$ model. Bisterzo et al. (2011) also studied HD 196944, and found the best match with a model of $M = 1.5 M_{\odot}$, with no initial enhancements of *r*-process elements.

The Bisterzo et al. (2010) models also calculate the evolution of *s*-process element abundances with $[\text{Fe}/\text{H}]$, which is a useful diagnostics for selecting AGB models with different masses and ^{13}C -pocket efficiencies. Figure 11 shows the $[\text{Pb}/\text{Fe}]$, $[\text{Ba}/\text{Fe}]$, and $[\text{Pb}/\text{Ba}]$ values for HD 196944 and HD 201626 compared with four of the model prescriptions from Bisterzo et al. (2010). The $[\text{Pb}/\text{Ba}]$ values for HD 196944 and HD 201626 are consistent with the *s*-process nucleosynthesis in low-mass low-metallicity AGB stars with the highest neutron exposures possible.

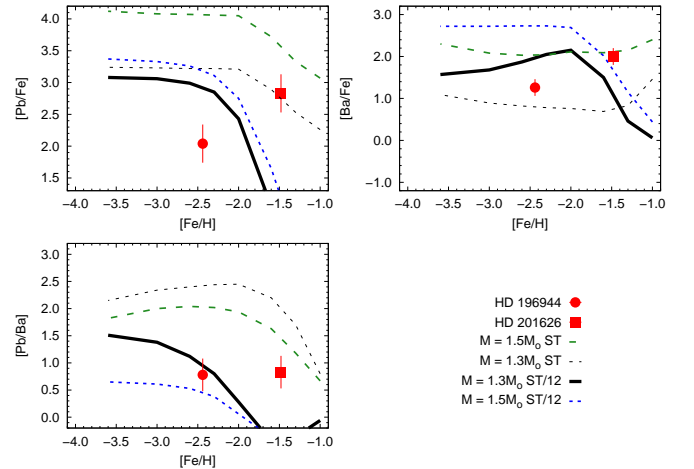


Figure 11. $[\text{Pb}/\text{Fe}]$, $[\text{Ba}/\text{Fe}]$, and $[\text{Pb}/\text{Ba}]$ compared with AGB theoretical predictions for two different initial masses and ^{13}C -pocket efficiencies. Data were taken from Tables B5 and B6 of Bisterzo et al. (2010).

Bisterzo et al. (2010) also point to the importance of measuring Nb abundances in CEMP stars, to distinguish between the *intrinsic* (star on the thermally-pulsing AGB or post-AGB phase) and *extrinsic* (main-sequence or red giant-branch star – CEMP-*s* stars). As noted by Wallerstein & Dominy (1988), an *intrinsic* AGB star is expected to be technetium-rich (Tc ; $Z=43$), ^{93}Zr -rich, and ^{93}Nb -poor, with $[\text{Zr}/\text{Nb}] \sim 1$. The *s*-process abundances of an *extrinsic* AGB star are the result of pol-

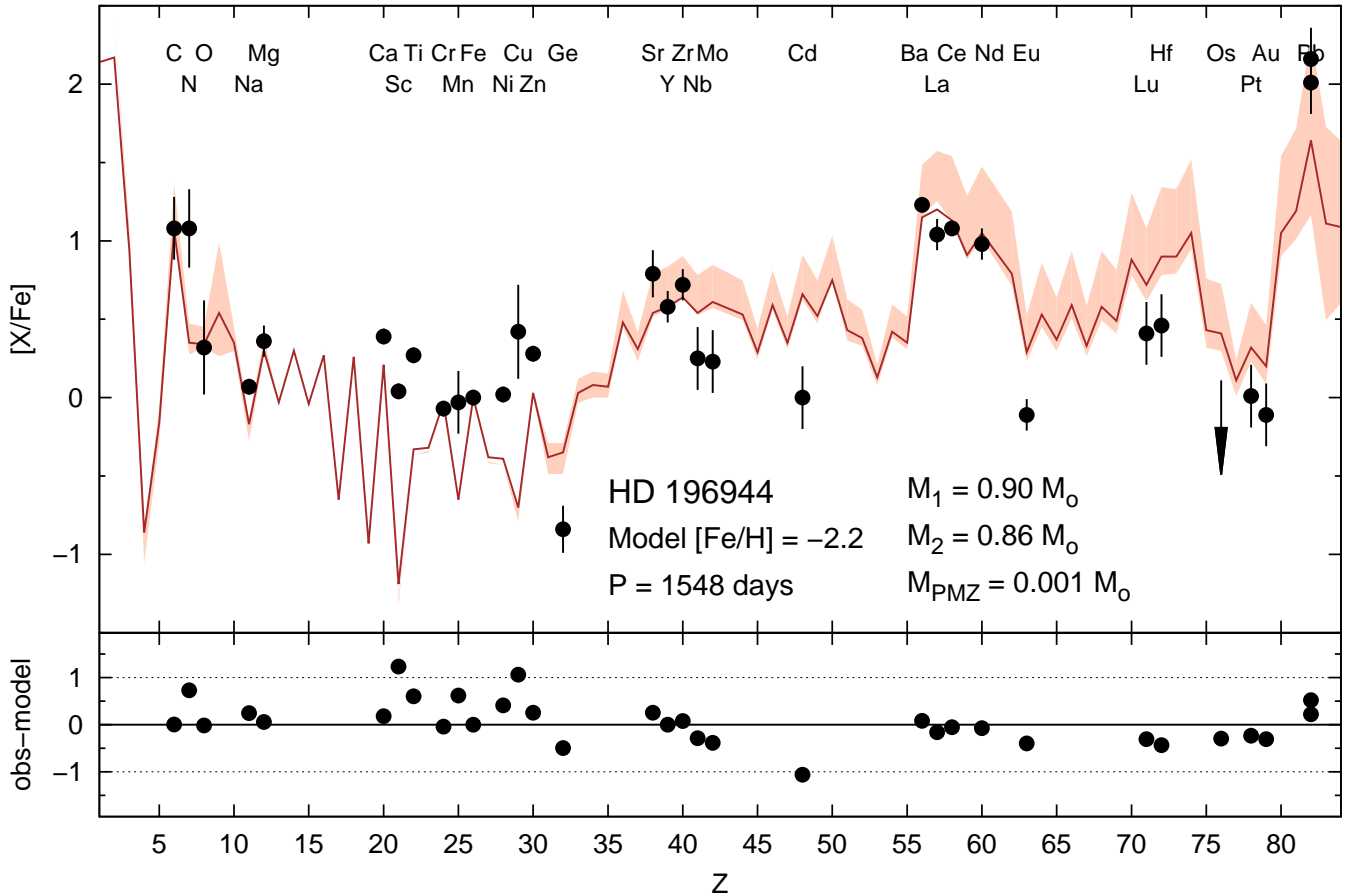


Figure 12. Upper panel: Model fitting for HD 196944. The black filled dots are abundances determined by this work, the solid line is the best-fitting model, and the shaded area represents the uncertainty on the model values (see Section 4.2 for details). Lower panel: Residuals computed as the difference between the observed and model abundances.

lution from a former AGB star onto the atmosphere of what once was the lower mass star in a binary system where the abundance of Nb (which has a single stable isotope) is a result of β -decay from ^{93}Zr , leading to $[\text{Zr}/\text{Nb}] \sim 0$ (see e.g. the CEMP- r/s star CS 29497–030, with $[\text{Zr}/\text{Nb}] = -0.27$, [Ivans et al. 2005](#)). For HD 196944, for which these two elemental abundances were derived from the NUV spectra, we find $[\text{Zr}/\text{Nb}] = +0.47 \pm 0.21$. However, we note that our Nb abundance is derived from the weak Nb II feature at 2950 Å.

4.2. Comparison with [Abate et al. \(2015a\)](#)

We also investigated the properties of HD 196944 and HD 201626 by comparing their derived elemental abundances with the grid of binary-evolution models of [Abate et al. \(2015a\)](#). This grid consists of about 290,000 binary stars distributed in the $M_1 - M_2 - \log_{10} a - M_{\text{PMZ}}$ parameter space, where $M_{1,2}$ are the initial masses of the primary and secondary stars, respectively, a is the initial orbital separation of the system, and M_{PMZ} is the mass of the partial-mixing zone. The mass of the partial-mixing zone is a parameter of the nucleosynthesis model that relates to the amount of free neutrons available for

neutron-capture processes in AGB stars²³. In this study we used model set B of [Abate et al. \(2015a\)](#), which allows efficient angular-momentum loss during mass transfer and large wind mass-accretion efficiencies over a wide range of orbital separations.

The best-fitting model to the observed abundances of each star is determined following [Abate et al. \(2015a\)](#). The model ages are selected between 10 Gyr and 13.7 Gyr, bracketing the expected ages of very metal-poor halo stars. The orbital periods of the models are chosen to reproduce the observed periods within the spatial resolution of our grid ($\Delta \log_{10}(a/R_{\odot}) = 0.1$, which corresponds to $\Delta \log_{10}(P_{\text{orb}}/\text{days}) = 0.15$). To constrain the evolutionary stage, we select model stars that reproduce the measured surface gravities within the observational uncertainties. For the model stars that fulfill these criteria, we determine the model that minimizes χ^2 , calculated by taking into account the abundances of the light elements up to atomic number 12 (Mg), and all neutron-capture elements from Ga ($Z=31$) to Pb ($Z=82$). The elements with atomic numbers between 13 (Al) and 30 (Zn) are not considered in the calculation of χ^2 , be-

²³ For details about the modelling of the partial-mixing zone and its role in AGB nucleosynthesis, we refer the interested reader to [Karakas \(2010\)](#); [Lugaro et al. \(2012\)](#); [Abate et al. \(2015a\)](#).

cause they are not in general produced by low-mass stars ($M < 3M_{\odot}$, see, e.g., [Karakas et al. 2009](#); [Cristallo et al. 2011](#)). In cases where only upper limits are available for a given element, an observational uncertainty of 0.3 dex is adopted to compute χ^2 , if the model abundance value is higher than the observed upper limit. This value was chosen because it is the largest observational uncertainty from our abundance determinations.

The initial abundances used in the models (up to Ge) are predicted by [Kobayashi et al. \(2011\)](#) in their models of Galactic chemical evolution at $[\text{Fe}/\text{H}] = -2.3$. For elements heavier than Ge, we use Solar System scaled values. It must be kept in mind that the impact of the choice of the initial set of abundances is negligible when studying CEMP-*s* stars. This is because the abundances of most key elements (e.g., C, N, Na, Mg, and all neutron-capture elements) have large variations during AGB evolution. The fit is made by combining the abundances of C and N. This is because, in giants, some amount of C is converted to N at the bottom of the convective envelope during dredge up. Even though the exact amount is very uncertain, the total C+N is conserved, therefore the total C+N predicted by the models is supposed to reproduce the observed abundance. For this comparison, we thus do not employ the carbon-abundance corrections, just the observed values.

Figures 12 and 13 show the best-fitting models for both HD 196944 ($M_{1,i} = 0.9M_{\odot}$, $M_{2,i} = 0.86M_{\odot}$, for $[\text{Fe}/\text{H}] = -2.2$), and HD 201626 ($M_{1,i} = 0.9M_{\odot}$, $M_{2,i} = 0.76M_{\odot}$, for $[\text{Fe}/\text{H}] = -2.2$; $M_{1,i} = 1.6M_{\odot}$, $M_{2,i} = 0.59M_{\odot}$, for $[\text{Fe}/\text{H}] = -1.5$) as solid lines. The abundances from this work are shown as filled dots with error bars. The shaded areas encompass the minimum and maximum abundances predicted by models that: (i) have an age between 10 Gyr and 13.7 Gyr; (ii) reproduce the observed period within the grid resolution and $\log g$ within the observational uncertainties; and (iii) have a final χ^2 that is less than three times the χ^2 of the best fit. For HD 201626, we ran two models, with metallicities $Z = 10^{-4}$ and 5×10^{-4} , which correspond to $[\text{Fe}/\text{H}] = -2.2$ and -1.5 , respectively, with the solar abundance set of [Asplund et al. \(2009\)](#). Also shown in the plot are the initial parameters of the best models ($[\text{Fe}/\text{H}]$, M_1 , M_2 , M_{PMZ}) and the final orbital period (given as input). Comments on the model-matching for each star are given below.

4.2.1. HD 196944

HD 196944 is a CEMP-*s* ($[\text{Ba}/\text{Eu}] = +1.33$) giant star with $[\text{Fe}/\text{H}] = -2.46$. This star has been the subject of many studies in the literature – SIMBAD notes 67 references. This star is known to be an extremely weak-lined G/K star with very strong CH bands ([Bidelman 1981](#)). For the model comparison, we used the abundances from both optical and NUV spectra, as well as the orbital period determined in this work. To test the robustness of the model-fitting procedure, we made a few experiments, removing abundances for elements mainly formed by the *r*-process (e.g., Eu, Lu, Os, Pt, and Au); the initial parameters adjusted with the routines did not change.

Inspection of Figure 12 reveals excellent agreement between the observations and model predictions for the light elements C, O, Na, Mg, Cr, and Fe. Some unexpected differences are found for N, Sc, and Ti. For ger-

manium, even though the abundance is ~ 0.5 dex lower than the model prediction, it is not a concern, since its abundance does not change much due to the main component of the *s*-process ([Pignatari et al. 2010](#); [Bisterzo et al. 2011](#); [Roederer 2012](#)).

For the first (Sr-Zr) and second (Ba-Nd) *s*-process peaks, all the abundances are within ~ 0.3 dex higher than the model. Other elements that are low compared to the model are: Cd, Eu, Pt, and Au. In the Solar System, 57% of Cd comes from the *s*-process ([Arlandini et al. 1999](#)); this element is not expected to be depleted. This is also supported empirically by the sub-solar $[\text{Cd}/\text{Fe}]$ ratios found in low-metallicity stars with *r*-process material ([Roederer et al. 2014b](#)), which implies that another (secondary) process must occur at later times or in higher-metallicity environments to bring the $[\text{Cd}/\text{Fe}]$ ratio up to the solar value.

For Eu, Au, and Pt, only 5-8% of their abundances are produced by the *s*-process. Therefore, it is unexpected that the (small) amount of these elements produced by the model with the *s*-process are higher than the observed values. This difference could be accounted for if we consider a sub-solar abundance of Eu (and accordingly Au and Pt) at low metallicity. However, it is worth mentioning that the previous Eu determination by [Aoki et al. \(2002\) – \$\log \epsilon\(\text{Eu}\) = -1.53\$ – is about 0.5 dex higher than the one from this work, and is in agreement with the models. Further observations are needed to reliably determine the abundances of these elements. Nevertheless, despite the discrepancies mentioned above, the overall model fits most of the observed abundances within \$\pm 0.5\$ dex.](#)

We can compare our best-fitting model of HD 196944 with the previous results obtained by [Abate et al. \(2015b\)](#). In this study, the same grid of models was used as in the present work, but no derived orbital period was available at the time to constrain the models. The orbital parameters found with model set B are $M_{1,i} = 1.2M_{\odot}$, $M_{2,i} = 0.79M_{\odot}$, $P_i = 6.9 \times 10^4$ days and $P_f = 4.6 \times 10^4$ days. As a consequence of the period constraint, our best model has a lower primary mass, a higher secondary mass, and shorter initial and final orbital periods, namely $M_{1,i} = 0.9M_{\odot}$, $M_{2,i} = 0.86M_{\odot}$, $P_i = 1.64 \times 10^3$ days and $P_f = 1.54 \times 10^3$ days. If we adopt a higher primary mass of $M_{1,i} = 1.2M_{\odot}$, no model in our grid reproduces the observed orbital period. Binary systems with initial periods shorter than about 3300 days experience a common-envelope phase as the primary star overfills its Roche lobe during the AGB phase, and consequently the final orbital periods are of the order of a few hundred days. Initially wider binary systems do not lose enough angular momentum, thus their orbital periods are much longer than the observed ($P_f > 3000$ days). In contrast, if we ignore the period constraint, our best-fitting model has essentially the same initial parameters as [Abate et al. \(2015b\)](#), $M_{1,i} = 1.2M_{\odot}$, $M_{2,i} = 0.79M_{\odot}$, $P_i = 9.8 \times 10^4$ days and $P_f = 6.4 \times 10^4$ days. However, the same regime of neutron-capture process operates in low-mass AGB stars ($M_{\text{AGB}} \leq 1.5M_{\odot}$; e.g., [Lugaro et al. 2012](#)), and consequently the *s*-element distributions do not vary significantly between our models at $M_{1,i} = 1.2M_{\odot}$ and $M_{1,i} = 0.9M_{\odot}$.

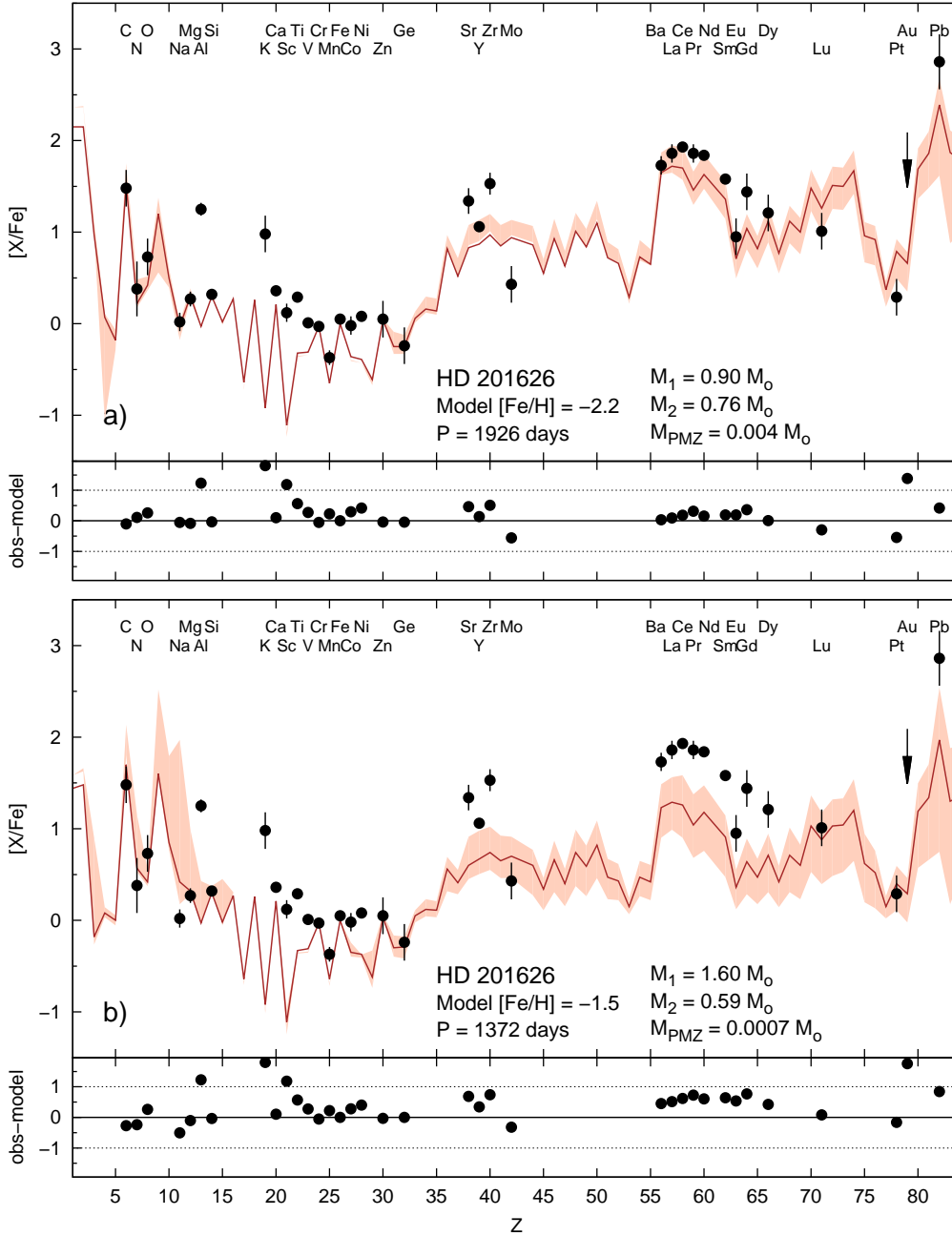


Figure 13. Same as Figure 12 and: a) with model metallicity of $Z = 10^{-4}$ (corresponding to $[Fe/H] \approx -2.2$). b) with model metallicity of $Z = 5 \cdot 10^{-4}$ ($[Fe/H] \approx -1.5$).

4.2.2. HD 201626

HD 201626 is a well-known CH star that has been extensively studied at optical wavelengths – SIMBAD notes 125 references. Originally discovered to be a CH star by Northcott (1953), the first spectroscopic chemical composition analysis (Wallerstein & Greenstein 1963) identified HD 201626 as being rich in C, Ba, La, Ce, and Nd. The authors noted that the abundances of these species provided “[...] evidence for *s*-process element formation in old stars of low metal content.” In this work we were able to add many new abundances for HD 201626. Particularly important are the abundances of Na and Mg, since these place strong constraints on the mass

and the M_{PMZ} of the AGB donor star (e.g., Abate et al. 2015a). Another important abundance determination is Eu, which is a indicator of the operation of the *r*-process. With this abundance, it is possible to calculate the ratio $[Ba/Eu] = +0.78$, which places HD 201626 in the CEMP-*s* sub-class, according to the the definition of Beers & Christlieb (2005).

The best-fit model calculated at metallicity $Z = 10^{-4}$ ($[Fe/H] = -2.2$; upper panels of Figure 13) shows good agreement with the observations. C, N, and O agree with the model within the observed uncertainties. Na, Mg, and Si are all within 0.05 dex from the model values. However, some elements, such as Al, K, Sc, Ti, and V exhibit large residuals when compared to the models. For

the elements in the first peak of the *s*-process (Sr, Y, Zr, Mo), there is a large spread, but the abundances are all within ± 0.5 dex from the model. The other elements, in particular the ones from the second peak of the *s*-process (Ba-Nd) are well-reproduced by the model. Similar to HD 196944, Pt is ~ 0.4 dex lower than the model. The Pb abundance, which is also an important constraint of *s*-process nucleosynthesis, is within 2σ of the model values.

The results are significantly worse when the model metallicity is $Z = 5 \cdot 10^{-4}$ ($[\text{Fe}/\text{H}] = -1.5$; lower panels of Figure 13), which would be, in principle, more appropriate for this star. This is likely due to a limitation of the models, since these were optimized to $[\text{Fe}/\text{H}] = -2.2$. The residuals for elements with $Z > 38$ all shifted to higher values, meaning that the model is underproducing *s*-process elements.

Abate et al. (2015a) also studied the abundance pattern of HD 201626, using chemical-abundance values from the literature. The authors determined a higher primary mass ($M_{1,i} = 2.6 M_{\odot}$, with the same model set B) than our best-fit model ($M_{1,i} = 0.9 M_{\odot}$), because the abundances of Na and Mg were undetermined at the time. Consequently, a relatively massive star with a large partial mixing zone ($M_{PMZ} = 4 \times 10^{-3} M_{\odot}$) well-reproduced the large observed enhancements of heavy-*s* elements and lead. This model also predicts high Na and Mg abundances ($[\text{Na}/\text{Fe}]_{\text{mod}} = +2.2$ and $[\text{Mg}/\text{Fe}]_{\text{mod}} = +1.5$), which are ruled out by our new observations, $[\text{Na}/\text{Fe}] = +0.02$, and $[\text{Mg}/\text{Fe}] = +0.27$.

5. CONCLUDING REMARKS

In this work we have presented abundance analyses of the NUV HST/STIS spectra of two bright CEMP-*s* stars, complemented by abundance determinations from optical Keck/HIRES spectra. Abundances for some of the elements measured in this work are only accessible from the NUV part of the spectra, and are of great importance for testing theoretical predictions of *s*-process nucleosynthesis. We also provided the first determination of the orbital period for HD 196944. We compared our results with models of AGB nucleosynthesis, as well as models for the evolution of binary systems containing CEMP stars. Results are in good agreement with the models, and are yet another confirmation of the formation scenario for the CEMP-*s* stars.

To our knowledge, this is the first attempt to match theoretical predictions of AGB evolution models and binary evolution with elemental abundances measured in the NUV. This opens a new window of opportunity for further high-resolution spectroscopy with HST/STIS for CEMP-*s* stars, which will help further constrain not only specific characteristics of AGB stars, but also for the evolution of the binary system in which these objects are found. To carry out such an effort, newly identified *bright* CEMP-*s* stars are required.

V.M.P., T.C.B., and H.S. acknowledge partial support for this work from PHY 08-22648; Physics Frontier Center/Joint Institute for Nuclear Astrophysics (JINA) and PHY 14-30152; Physics Frontier Center/JINA Center for the Evolution of the Elements (JINA-CEE), awarded by the US National Science Foundation. T. H. was supported by Sonderforschungsbereich SFB 881 "The Milky

Way System" (subproject A4) of the German Research Foundation (DFG). A.F. is supported by NSF CAREER grant AST-1255160. W.A. was supported by the JSPS Grants-in-Aid for Scientific Research (23224004). Generous support for Program GO-12554 has been provided by NASA through a grant from the Space Telescope Science Institute, which is operated by the Association of Universities for Research in Astronomy, Inc., under NASA contract NAS 5-26555. This research has made use of the Keck Observatory Archive, which is operated by the W. M. Keck Observatory and the NASA Exoplanet Science Institute, under contract with the National Aeronautics and Space Administration; the SIMBAD database, operated at CDS, Strasbourg, France; and the NASA/IPAC Infrared Science Archive, which is operated by the Jet Propulsion Laboratory, California Institute of Technology, under contract with the National Aeronautics and Space Administration. The authors also wish to recognize and acknowledge the very significant cultural role and reverence that the summit of Mauna Kea has always had within the indigenous Hawaiian community. We are most fortunate to have the opportunity to conduct observations from this mountain.

Facilities: HST (STIS), Keck:II (HIRES)

REFERENCES

- Abate, C., Pols, O. R., Izzard, R. G., Mohamed, S. S., & de Mink, S. E. 2013, *A&A*, 552, A26
- Abate, C., Pols, O. R., Karakas, A. I., & Izzard, R. G. 2015, *A&A*, 576, A118
- Abate, C., Pols, O. R., Izzard, R. G., & Karakas, A. I. 2015, *arXiv:1507.04662*
- Abate, C., Pols, O. R., Stancliffe, R. J., et al. 2015, *arXiv:1507.04969*
- Andersson, M., Gruner, J., Ryde, N., et al. 2015, *ApJS*, 216, 2
- Anderton, T. R. 2015, PhD thesis, in prep.
- Aoki, W., Frebel, A., Christlieb, N., et al. 2006, *ApJ*, 639, 897
- Aoki, W., Ryan, S. G., Norris, J. E., et al. 2002, *ApJ*, 580, 1149
- Aoki, W., & Tsuji, T. 1997, *A&A*, 317, 845
- Arlandini, C., Käppeler, F., Wisshak, K., et al. 1999, *ApJ*, 525, 886
- Asplund, M. 2005, *ARA&A*, 43, 481
- Asplund, M., Grevesse, N., Sauval, A. J., & Scott, P. 2009, *ARA&A*, 47, 481
- Barnbaum, C., Stone, R. P. S., & Keenan, P. C. 1996, *ApJS*, 105, 419
- Beers, T. C., & Christlieb, N. 2005, *ARA&A*, 43, 531
- Bergeson, S. D., & Lawler, J. E. 1993, *ApJ*, 408, 382
- Bidelman, W. P. 1981, *AJ*, 86, 553
- Biémont, E., Garnir, H. P., Palmeri, P., Li, Z. S., & Svanberg, S. 2000, *MNRAS*, 312, 116
- Bisterzo, S., Gallino, R., Straniero, O., Cristallo, S., & Käppeler, F. 2010, *MNRAS*, 404, 1529
- . 2011, *MNRAS*, 418, 284
- . 2012, *MNRAS*, 422, 849
- Blackwell, D. E., Petford, A. D., & Shallis, M. J. 1980, *A&A*, 82, 249
- Blackwell-Whitehead, R., & Bergemann, M. 2007, *A&A*, 472, L43
- Buchhave, L. A., Bakos, G. Á., Hartman, J. D., et al. 2010, *ApJ*, 720, 1118
- Calamida, A., Bono, G., Stetson, P. B., et al. 2007, *ApJ*, 670, 400
- Casagrande, L., Schonrich, R., Asplund, M., et al. 2011, *A&A*, 530, 138+21
- Castelli, F., & Kurucz, R. L. 2004, *ArXiv Astrophysics e-prints*, *arXiv:astro-ph/0405087*
- Collet, R., Asplund, M., & Trampedach, R. 2007, *A&A*, 469, 687
- Cowan, J. J., Sneden, C., Beers, T. C., et al. 2005, *ApJ*, 627, 238
- Cristallo, S., Piersanti, L., Straniero, O., et al. 2011, *ApJS*, 197, 17
- Den Hartog, E. A., Herd, M. T., Lawler, J. E., et al. 2005, *ApJ*, 619, 639

- Den Hartog, E. A., Lawler, J. E., Sobeck, J. S., Sneden, C., & Cowan, J. J. 2011, *ApJS*, 194, 35
- Fabbian, D., Asplund, M., Barklem, P. S., Carlsson, M., & Kiselman, D. 2009, *A&A*, 500, 1221
- Fedchak, J. A., & Lawler, J. E. 1999, *ApJ*, 523, 734
- Fitzpatrick, M. J., & Sneden, C. 1987, in *Bulletin of the American Astronomical Society*, Vol. 19, *Bulletin of the American Astronomical Society*, 1129
- Fivet, V., Quinet, P., Biémont, É., & Xu, H. L. 2006, *Journal of Physics B Atomic Molecular Physics*, 39, 3587
- Frebel, A., & Norris, J. E. 2015, *ArXiv e-prints*, arXiv:1501.06921
- Fuhr, J. R., & Wiese, W. L. 2009, published in the *CRC Handbook of Chemistry and Physics*
- Garcia Perez, A. E., Asplund, M., Primas, F., Nissen, P. E., & Gustafsson, G. 2006, *A&A*, 451, 621
- Hauck, B., & Mermilliod, M. 1997, *VizieR Online Data Catalog*, 2215, 0
- Ivans, I. I., Simmerer, J., Sneden, C., et al. 2006, *ApJ*, 645, 613
- Ivans, I. I., Sneden, C., Gallino, R., Cowan, J. C., & Preston, G. W. 2005, *ApJ*, 627, L145
- Ivans, I. I., Sneden, C., James, C. R., et al. 2003, *ApJ*, 592, 906
- Karakas, A. I. 2010, *MNRAS*, 403, 1413
- Karakas, A. I., van Raai, M. A., Lugaro, M., Sterling, N. C., & Dinerstein, H. L. 2009, *ApJ*, 690, 1130
- Karinkuzhi, D., & Goswami, A. 2014, *MNRAS*, 440, 1095
- Kimble, R. A., Woodgate, B. E., Bowers, C. W., et al. 1998, *ApJ*, 492, L83
- Kobayashi, C., Karakas, A. I., & Umeda, H. 2011, *MNRAS*, 414, 3231
- Kraft, R. P., & Ivans, I. I. 2003, *PASP*, 115, 143
- . 2004, *Origin and Evolution of the Elements*, 33
- Kramida, A., Yu. Ralchenko, Reader, J., & and NIST ASD Team. 2013, *NIST Atomic Spectra Database* (ver. 5.1), [Online]. Available: <http://physics.nist.gov/asd> [2014, April 7]. National Institute of Standards and Technology, Gaithersburg, MD.
- Kupka, F., Piskunov, N., Ryabchikova, T. A., Stempels, H. C., & Weiss, W. W. 1999, *A&AS*, 138, 119
- Kurucz, R. L. 1993, *Kurucz CD-ROM*, Cambridge, MA: Smithsonian Astrophysical Observatory, —c1993, December 4, 1993
- Kurucz, R., & Bell, B. 1995, *Atomic Line Data* (R.L. Kurucz and B. Bell) *Kurucz CD-ROM No. 23*. Cambridge, Mass.: Smithsonian Astrophysical Observatory, 1995., 23
- Lawler, J. E., den Hartog, E. A., Labby, Z. E., et al. 2007, *ApJS*, 169, 120
- Lawler, J. E., Wood, M. P., Den Hartog, E. A., et al. 2014, *ApJS*, 215, 20
- Ljung, G., Nilsson, H., Asplund, M., & Johansson, S. 2006, *A&A*, 456, 1181
- Lucatello, S., Tsangarides, S., Beers, T. C., et al. 2005, *ApJ*, 625, 825
- Lugaro, M., Karakas, A. I., Stancliffe, R. J., & Rijs, C. 2012, *ApJ*, 747, 2
- Malcheva, G., Blagoev, K., Mayo, R., et al. 2006, *MNRAS*, 367, 754
- Mashonkina, L., Ryabtsev, A., & Frebel, A. 2012, *A&A*, 540, A98
- McClure, R. D., & Woodsworth, A. W. 1990, *ApJ*, 352, 709
- McDonald, I., Zijlstra, A. A., & Boyer, M. L. 2012, *MNRAS*, 427, 343
- Meléndez, J., & Barbuy, B. 2009, *A&A*, 497, 611
- Morton, D. C. 2000, *ApJS*, 130, 403
- Nilsson, H., & Ivarsson, S. 2008, *A&A*, 492, 609
- Nordström, B., Mayor, M., Andersen, J., et al. 2004, *A&A*, 418, 989
- Northcott, R. J. 1953, *JRASC*, 47, 65
- Pál, A. 2009, *MNRAS*, 396, 1737
- Pignatari, M., Gallino, R., Heil, M., et al. 2010, *ApJ*, 710, 1557
- Placco, V. M., Frebel, A., Beers, T. C., et al. 2013, *ApJ*, 770, 104
- Placco, V. M., Frebel, A., Beers, T. C., & Stancliffe, R. J. 2014a, *ApJ*, 797, 21
- Placco, V. M., Beers, T. C., Roederer, I. U., et al. 2014b, *ApJ*, 790, 34
- Quinet, P., Palmeri, P., Biémont, É., et al. 2006, *A&A*, 448, 1207
- Ramirez, I., Allende Prieto, C., & Lambert, D. L. 2013, *ApJ*, 764, 78
- Ramirez, I., & Melendez, J. 2005, *ApJ*, 743, 465
- Roederer, I. U. 2012, *ApJ*, 756, 36
- Roederer, I. U., Cowan, J. J., Karakas, A. I., et al. 2010, *ApJ*, 724, 975
- Roederer, I. U., Kratz, K., Frebel, A., et al. 2009, *ApJ*, 698, 1963
- Roederer, I. U., Lawler, J. E., Sneden, C., et al. 2008, *ApJ*, 675, 723
- Roederer, I. U., Preston, G. W., Thompson, I. B., et al. 2014a, *AJ*, 147, 136
- Roederer, I. U., Lawler, J. E., Sobeck, J. S., et al. 2012, *ApJS*, 203, 27
- Roederer, I. U., Schatz, H., Lawler, J. E., et al. 2014b, *ApJ*, 791, 32
- Ruffoni, M. P., Den Hartog, E. A., Lawler, J. E., et al. 2014, *MNRAS*, 44, 3127
- Schlafly, E. F., & Finkbeiner, D. P. 2011, *ApJ*, 737, 103
- Sikström, C. M., Pihlmark, H., Nilsson, H., et al. 2001, *Journal of Physics B Atomic Molecular Physics*, 34, 477
- Simmerer, J., Ivans, I. I., Filler, D., et al. 2013, *ApJ*, 764, L7
- Siqueira Mello, C., Spite, M., Barbuy, B., et al. 2013, *A&A*, 550, A122
- Sneden, C., Lucatello, S., Ram, R. S., Brooke, J. S. A., & Bernath, P. 2014, *ApJS*, 214, 26
- Sneden, C., Cowan, J. J., Lawler, J. E., et al. 2003, *ApJ*, 591, 936
- Sneden, C. A. 1973, PhD thesis, The University of Texas at Austin.
- Sobeck, J. S., Kraft, R. P., Sneden, C., et al. 2011, *AJ*, 141, 175
- Takeda, Y. 2003, *A&A*, 402, 343
- Van Eck, S., Goriely, S., Jorissen, A., & Plez, B. 2003, *A&A*, 404, 291
- Vanture, A. D. 1992, *AJ*, 103, 2035
- Vogt, S. S., Allen, S. L., Bigelow, B. C., et al. 1994, in *Society of Photo-Optical Instrumentation Engineers (SPIE) Conference Series*, Vol. 2198, *Instrumentation in Astronomy VIII*, ed. D. L. Crawford & E. R. Craine, 362
- Wallerstein, G., & Dominy, J. F. 1988, *ApJ*, 330, 937
- Wallerstein, G., & Greenstein, J. L. 1963, *AJ*, 68, 546
- . 1964, *ApJ*, 139, 1163
- Waters, C. Z., & Hollek, J. K. 2013, *PASP*, 125, 1164
- Wenger, M., Ochsenbein, F., Egret, D., et al. 2000, *A&AS*, 143, 9
- Wood, M. P., Lawler, J. E., Den Hartog, E. A., Sneden, C., & Cowan, J. J. 2014a, *ApJS*, 214, 18
- Wood, M. P., Lawler, J. E., Sneden, C., & Cowan, J. J. 2013, *ApJS*, 208, 27
- . 2014b, *ApJS*, 211, 20
- Woodgate, B. E., Kimble, R. A., Bowers, C. W., et al. 1998, *PASP*, 110, 1183
- Zacs, L., Nissen, P. E., & Schuster, W. J. 1998, *A&A*, 337, 216
- Zinn, R., & West, M. J. 1984, *ApJS*, 55, 45

Table 1
Atmospheric Parameters

T_{eff} (K)	$\log g$ (cgs)	[Fe/H]	ξ (km s ⁻¹)	Method	Reference
HD 196944 (literature)					
5170	1.60	-2.41	1.55	a	This work
5250	1.70	-2.45	1.90	a	Zacs et al. (1998)
5250	1.80	-2.25	1.70	a	Aoki et al. (2002)
...	...	-2.40	...	a	Van Eck et al. (2003)
5170	1.80	-2.46	1.70	a	Roederer et al. (2008)
5310	1.75	-2.39	1.65	a	Roederer et al. (2014a)
HD 201626 (literature)					
5175	2.80	-1.51	1.30	a	This work
5190	2.25	-1.30	2.30	a	Vanture (1992)
4800	2.00	-1.50	2.00	b	Aoki & Tsuji (1997)
5120	2.25	-1.40	1.02	a	Karinkuzhi & Goswami (2014)
4800	1.30	-1.90	2.00	c	Snedden et al. (2014)
4550	d	Casagrande et al. (2011)
4852	e	McDonald et al. (2012)
HD 201626 (additional color-based estimates)					
4561 [*]	c	$B - V$ from Wenger et al. (2000)
4593 [*]	c	$ubvy$ from Hauck & Mermilliod (1997)
4971 [*]	c	V from Wenger et al. (2000); K from 2MASS
...	...	-1.29 [*]	...	f	$ubvy$ from Hauck & Mermilliod (1997)
...	...	-1.59 [*]	...	g	$ubvy$ from Hauck & Mermilliod (1997)
...	...	-1.23 [*]	...	f,h	$ubvy$ from Hauck & Mermilliod (1997)
...	...	-1.53 [*]	...	g,h	$ubvy$ from Hauck & Mermilliod (1997)

Note. —

- (a) Spectroscopic constraints
- (b) IRFM (Blackwell et al. 1980)
- (c) color-Teff (Ramirez & Melendez 2005)
- (d) color-Teff (Casagrande et al. 2011)
- (e) SED modelling
- (f) $ubvy$ -metallicity (Calamida et al. 2007); empirical relation
- (g) $ubvy$ -metallicity (Calamida et al. 2007); theoretical relation
- (h) converted to Kraft & Ivans (2003, 2004) metallicity scale

^{*} Estimates made by adopting the $E(B - V)$ value based on the dust maps of Schlafly & Finkbeiner (2011) at the IRSA Galactic Dust Reddening and Extinction Service^a. However, as noted by Sneden et al. (2014), because the star is only some 300 pc away, one would expect to see a smaller dereddening effect from a fraction of the total $E(B - V)$ value (and thus, an even cooler photometric color- T_{eff}).

^a <http://irsa.ipac.caltech.edu/applications/DUST/>

Table 2
Derived Optical Abundance Estimates

Ion	λ (Å)	χ (eV)	$\log gf$	$\log \epsilon$ (X) HD 196944	$\log \epsilon$ (X) HD 201626
Equivalent width analysis					
C I	4771.75	7.49	-1.87	...	8.56
C I	5380.34	7.68	-1.62	...	8.26
C I	6587.61	8.54	-1.00	...	8.11
Na I	5682.63	2.10	-0.70	<4.10	...
Na I	5688.19	2.10	-1.40	3.90	4.50
Na I	6160.75	2.10	-1.25	...	5.01
Mg I	4571.10	0.00	-5.57	5.34	6.39
Mg I	4702.99	4.34	-0.44	5.61	...
Mg I	5172.69	2.71	-0.45	5.74	...
Mg I	5183.60	2.72	-0.24	5.68	...
Mg I	5528.42	4.35	-0.34	5.47	6.26
Mg I	5711.09	4.34	-1.63	5.46	6.21
Mg I	6318.72	5.11	-2.10	...	6.57
Al I	6631.22	4.02	-1.70	...	6.13
Al I	6906.29	4.02	-1.13	...	6.26
Si I	4782.99	4.95	-1.76	...	6.46
Si I	5493.88	5.61	-0.62	...	6.18
Si I	5645.61	4.93	-2.14	...	6.47
Si I	5669.74	5.62	-1.34	...	6.11
Si I	5675.42	5.62	-1.03	...	6.19
Si I	5690.43	4.93	-1.87	...	6.14
Si I	5948.55	5.08	-1.23	...	6.49
Si I	6106.61	5.61	-1.73	...	6.35

Table 2 — *Continued*

Ion	λ (Å)	χ (eV)	$\log gf$	$\log \epsilon$ (X) HD 196944	$\log \epsilon$ (X) HD 201626
Si I	6112.93	5.61	-1.75	...	6.40
Si I	6131.57	5.61	-1.20	...	6.48
Si I	6142.49	5.62	-1.48	...	6.43
Si I	6155.69	5.62	-1.69	...	6.30
Si I	6244.48	5.61	-1.27	...	6.43
Si I	6976.51	5.95	-1.17	...	6.29
Si I	7003.57	5.96	-0.97	...	6.44
Si I	7034.90	5.87	-0.88	...	6.35
Si I	7164.69	5.87	-1.30	...	6.29
Si I	7226.21	5.61	-1.51	...	6.53
Si I	7235.33	5.61	-1.50	...	6.20
Si I	7250.63	5.62	-1.04	...	6.11
Si I	7275.29	5.61	-1.00	...	6.40
Si I	7289.18	5.62	-0.20	...	6.52
Si I	7409.08	5.61	-0.88	...	6.08
Si I	7742.72	6.20	-0.28	...	6.23
Si I	7932.35	5.96	-0.47	...	6.33
Si I	7970.31	5.96	-1.47	...	6.49
K I	7698.96	0.00	-0.18	...	4.38
Ca I	5265.56	2.52	-0.26	4.49	...
Ca I	5349.47	2.71	-0.31	4.18	4.96
Ca I	5581.98	2.52	-0.56	4.24	...
Ca I	5588.76	2.53	0.36	4.26	5.03
Ca I	5590.12	2.51	-0.71	4.40	5.19
Ca I	5598.49	2.52	-0.22	4.40	...
Ca I	5857.46	2.93	0.24	4.29	5.13
Ca I	6102.73	1.88	-0.79	...	5.07
Ca I	6122.23	1.89	-0.32	...	5.20
Ca I	6161.30	2.52	-1.27	...	5.34
Ca I	6162.18	1.90	-0.09	...	5.17
Ca I	6166.44	2.52	-1.14	...	5.17
Ca I	6169.04	2.52	-0.80	...	5.30
Ca I	6169.56	2.52	-0.48	...	5.14
Ca I	6439.08	2.53	0.39	...	5.24
Ca I	6455.60	2.52	-1.29	...	5.44
Ca I	6471.66	2.51	-0.69	...	5.22
Ca I	6493.79	2.52	-0.11	...	5.17
Ca I	7148.15	2.71	0.14	...	5.29
Sc II	4400.40	0.61	-0.54	...	1.22
Sc II	4415.56	0.60	-0.67	...	2.09
Sc II	4670.41	1.36	-0.58	...	1.16
Sc II	5031.01	1.36	-0.40	0.71	...
Sc II	5239.81	1.46	-0.77	0.80	...
Sc II	5318.37	1.36	-2.01	...	1.84
Sc II	5526.78	1.77	0.02	0.75	...
Sc II	5640.99	1.50	-1.13	...	1.96
Sc II	5657.88	1.51	-0.60	0.86	1.92
Sc II	5667.15	1.50	-1.36	...	1.92
Sc II	6245.62	1.51	-1.07	...	1.96
Sc II	6279.74	1.50	-1.16	...	1.64
Sc II	6604.58	1.36	-1.31	...	1.91
Ti I	4453.31	1.43	-0.03	...	3.43
Ti I	4457.43	1.46	0.26	...	3.93
Ti I	4465.81	1.74	-0.13	...	3.75
Ti I	4512.73	0.84	-0.40	2.84	3.63
Ti I	4518.02	0.83	-0.25	...	3.92
Ti I	4522.80	0.82	-0.27	...	3.75
Ti I	4533.24	0.85	0.54	2.74	3.46
Ti I	4534.78	0.84	0.35	2.74	3.76
Ti I	4535.57	0.83	0.14	2.79	...
Ti I	4548.76	0.83	-0.28	2.82	3.51
Ti I	4555.48	0.85	-0.40	2.83	3.77
Ti I	4617.27	1.75	0.44	...	3.73
Ti I	4623.10	1.74	0.16	2.70	...
Ti I	4639.36	1.74	-0.05	...	3.98
Ti I	4656.47	0.00	-1.29	2.68	...
Ti I	4681.91	0.05	-1.03	2.74	...
Ti I	4840.87	0.90	-0.43	2.82	3.68
Ti I	4870.12	2.25	0.44	2.97	...
Ti I	4885.08	1.89	0.41	2.83	3.49
Ti I	4981.73	0.85	0.57	2.78	...
Ti I	4991.07	0.84	0.45	2.79	...
Ti I	5007.21	0.82	0.17	3.02	...
Ti I	5016.16	0.85	-0.48	2.75	...
Ti I	5020.03	0.84	-0.33	2.84	...

Table 2 — *Continued*

Ion	λ (Å)	χ (eV)	$\log gf$	$\log \epsilon$ (X) HD 196944	$\log \epsilon$ (X) HD 201626
Ti I	5022.87	0.83	−0.33	2.86	...
Ti I	5024.84	0.82	−0.53	2.81	...
Ti I	5035.90	1.46	0.22	2.94	...
Ti I	5064.65	0.05	−0.94	2.77	...
Ti I	5173.74	0.00	−1.06	2.78	...
Ti I	5210.38	0.05	−0.82	2.73	3.93
Ti I	5295.77	1.07	−1.59	...	3.81
Ti I	5471.19	1.44	−1.42	...	3.87
Ti I	5490.15	1.46	−0.84	...	3.49
Ti I	5512.52	1.46	−0.40	...	3.76
Ti I	5662.15	2.31	−0.05	...	3.46
Ti I	5866.45	1.07	−0.79	...	3.72
Ti I	5899.29	1.05	−1.10	...	3.60
Ti I	5918.54	1.07	−1.64	...	3.75
Ti I	5922.11	1.05	−1.38	...	3.77
Ti I	5953.17	1.89	−0.27	...	3.66
Ti I	6258.10	1.44	−0.39	...	3.75
Ti I	6258.71	1.46	−0.28	...	3.95
Ti I	6261.10	1.43	−0.53	...	3.83
Ti I	6861.44	2.27	−0.73	...	3.95
Ti I	7188.57	1.43	−1.71	...	4.05
Ti I	7244.85	1.44	−0.70	...	3.61
Ti I	7251.71	1.43	−0.76	...	3.65
Ti II	4395.84	1.24	−1.93	...	3.75
Ti II	4409.52	1.23	−2.53	...	3.82
Ti II	4432.10	1.24	−3.08	...	3.91
Ti II	4443.80	1.08	−0.71	...	3.93
Ti II	4450.48	1.08	−1.52	...	3.78
Ti II	4488.32	3.12	−0.50	...	3.38
Ti II	4501.27	1.12	−0.77	3.01	3.80
Ti II	4518.33	1.08	−2.56	2.87	4.07
Ti II	4524.68	1.23	−2.69	2.61	...
Ti II	4529.48	1.57	−1.75	2.90	3.94
Ti II	4544.02	1.24	−2.58	2.98	...
Ti II	4545.13	1.13	−2.45	2.69	...
Ti II	4563.76	1.22	−0.69	2.90	3.75
Ti II	4571.97	1.57	−0.31	3.03	...
Ti II	4583.41	1.17	−2.84	2.84	3.82
Ti II	4589.95	1.24	−1.79	...	3.90
Ti II	4609.27	1.18	−3.32	2.76	...
Ti II	4636.32	1.16	−3.02	2.73	...
Ti II	4657.20	1.24	−2.29	2.79	3.62
Ti II	4708.66	1.24	−2.35	2.79	...
Ti II	4763.88	1.22	−2.40	2.97	...
Ti II	4764.52	1.24	−2.69	2.74	3.78
Ti II	4798.53	1.08	−2.66	2.81	...
Ti II	4849.17	1.13	−2.96	3.09	...
Ti II	4865.61	1.12	−2.70	2.77	3.73
Ti II	4911.19	3.12	−0.64	2.76	...
Ti II	5005.17	1.57	−2.73	2.77	...
Ti II	5013.69	1.58	−2.14	2.81	...
Ti II	5129.16	1.89	−1.34	2.78	...
Ti II	5154.07	1.56	−1.75	2.77	...
Ti II	5185.90	1.89	−1.41	2.78	3.76
Ti II	5211.53	2.59	−1.41	...	3.65
Ti II	5226.54	1.56	−1.26	2.76	4.02
Ti II	5268.61	2.60	−1.61	...	3.77
Ti II	5336.79	1.58	−1.60	2.78	...
Ti II	5381.02	1.57	−1.97	2.81	...
Ti II	5396.25	1.58	−3.18	...	3.58
Ti II	5418.77	1.58	−2.13	2.80	...
Ti II	5490.69	1.56	−2.43	...	3.56
Ti II	5492.88	1.58	−2.93	...	3.66
Ti II	6491.56	2.06	−1.89	...	3.65
Ti II	6827.94	3.10	−1.99	...	4.14
Ti II	7004.67	3.09	−1.89	...	4.06
V I	6216.37	0.28	−1.07	...	2.43
Cr I	4545.95	0.94	−1.37	3.11	...
Cr I	4545.96	0.94	−1.38	...	4.15
Cr I	4580.06	0.94	−1.64	...	4.31
Cr I	4591.39	0.97	−1.74	...	3.97
Cr I	4600.74	1.00	−1.25	3.05	4.08
Cr I	4613.36	0.96	−1.65	3.47	...
Cr I	4616.12	0.98	−1.19	3.06	...
Cr I	4626.17	0.97	−1.33	3.11	4.14

Table 2 — *Continued*

Ion	λ (Å)	χ (eV)	$\log gf$	$\log \epsilon$ (X) HD 196944	$\log \epsilon$ (X) HD 201626
Cr I	4646.15	1.03	-0.74	3.07	3.91
Cr I	4651.28	0.98	-1.46	3.06	...
Cr I	4652.15	1.00	-1.04	3.14	...
Cr I	4708.02	3.17	0.07	3.37	...
Cr I	5204.52	0.94	-0.21	3.42	...
Cr I	5206.04	0.94	0.03	3.09	4.05
Cr I	5247.56	0.96	-1.63	3.08	4.04
Cr I	5264.15	0.97	-1.29	3.50	...
Cr I	5296.69	0.98	-1.36	3.10	...
Cr I	5297.36	2.90	0.17	3.14	3.94
Cr I	5300.74	0.98	-2.00	...	3.90
Cr I	5329.17	2.91	-0.06	...	4.12
Cr I	5345.80	1.00	-0.95	3.09	4.38
Cr I	5348.31	1.00	-1.21	3.01	4.02
Cr I	5409.77	1.03	-0.67	3.05	4.30
Cr I	5785.00	3.32	-0.38	...	4.11
Cr I	5787.99	3.32	-0.08	...	4.15
Cr I	7400.21	2.90	-0.11	...	4.46
Cr II	4554.99	4.07	-1.37	3.41	...
Cr II	4558.65	4.07	-0.66	3.47	...
Cr II	4588.20	4.07	-0.83	3.42	...
Cr II	4592.05	4.07	-1.42	3.48	...
Cr II	4618.80	4.07	-1.00	3.43	...
Cr II	4634.07	4.07	-0.98	3.14	...
Cr II	4848.23	3.86	-1.00	3.14	3.97
Cr II	4864.33	3.86	-1.37	...	3.99
Cr II	4876.40	3.85	-1.46	3.43	4.14
Cr II	5237.33	4.07	-1.16	3.27	4.20
Mn I	4709.70	2.88	-0.34	3.39	...
Mn I	4727.48	2.92	-0.47	3.38	...
Mn I	4754.02	2.27	-0.09	2.61	3.63
Mn I	4761.51	2.95	-0.14	...	3.18
Mn I	4766.42	2.92	0.10	...	3.47
Mn I	4783.39	2.29	0.04	2.60	...
Mn I	5394.62	0.00	-3.50	...	3.26
Mn I	5394.67	0.00	-3.50	...	3.41
Mn I	5407.42	2.14	-1.74	...	3.85
Mn I	5432.51	0.00	-3.79	...	3.85
Mn I	6016.64	3.06	-0.25	...	3.51
Mn I	6021.79	3.06	-0.12	...	3.82
Fe I	4365.90	2.99	-2.25	...	6.00
Fe I	4389.24	0.05	-4.58	...	6.03
Fe I	4423.84	3.66	-1.58	...	6.15
Fe I	4433.22	3.66	-0.73	...	6.21
Fe I	4443.19	2.86	-1.04	...	5.84
Fe I	4461.65	0.09	-3.21	...	6.17
Fe I	4489.74	0.12	-3.97	...	6.29
Fe I	4531.15	1.49	-2.16	5.04	6.13
Fe I	4602.00	1.61	-3.15	...	5.89
Fe I	4602.95	1.49	-2.21	5.07	...
Fe I	4619.29	3.60	-1.08	5.11	...
Fe I	4630.12	2.28	-2.59	5.17	...
Fe I	4638.01	3.60	-1.12	5.28	...
Fe I	4647.43	2.95	-1.35	5.12	...
Fe I	4704.95	3.69	-1.53	5.45	...
Fe I	4736.77	3.21	-0.75	5.21	...
Fe I	4776.07	3.30	-2.65	...	6.32
Fe I	4786.81	3.02	-1.61	5.11	...
Fe I	4859.70	2.88	-0.76	4.98	...
Fe I	4871.32	2.87	-0.36	5.05	5.97
Fe I	4872.14	2.88	-0.57	5.02	...
Fe I	4890.75	2.88	-0.39	5.17	6.07
Fe I	4891.49	2.85	-0.11	5.06	5.85
Fe I	4903.32	2.88	-0.93	5.05	...
Fe I	4918.99	2.87	-0.34	5.06	...
Fe I	4924.77	2.28	-2.11	5.05	...
Fe I	4994.13	0.92	-3.08	5.10	...
Fe I	5001.87	3.88	0.05	4.95	...
Fe I	5002.79	3.40	-1.53	5.20	...
Fe I	5014.94	3.94	-0.30	5.11	...
Fe I	5049.83	2.28	-1.35	5.05	...
Fe I	5051.64	0.92	-2.76	5.07	...
Fe I	5068.77	2.94	-1.04	5.03	...
Fe I	5074.75	4.22	-0.23	5.30	...
Fe I	5079.74	0.99	-3.22	5.22	...

Table 2 — *Continued*

Ion	λ (Å)	χ (eV)	$\log gf$	$\log \epsilon$ (X) HD 196944	$\log \epsilon$ (X) HD 201626
Fe I	5083.34	0.96	-2.96	5.08	...
Fe I	5110.44	0.00	-3.76	5.11	...
Fe I	5123.72	1.01	-3.07	5.27	...
Fe I	5125.12	4.22	-0.08	5.15	...
Fe I	5127.36	0.92	-3.31	5.06	...
Fe I	5131.48	2.22	-2.52	5.18	...
Fe I	5133.69	4.18	0.20	5.19	...
Fe I	5141.74	2.43	-2.24	5.08	...
Fe I	5151.91	1.01	-3.32	5.16	...
Fe I	5162.28	4.18	0.02	5.23	...
Fe I	5166.28	0.00	-4.12	4.97	...
Fe I	5171.59	1.49	-1.79	5.10	6.15
Fe I	5192.35	3.00	-0.42	4.97	...
Fe I	5194.95	1.56	-2.02	5.01	...
Fe I	5197.94	4.30	-1.62	...	6.31
Fe I	5198.71	2.22	-2.13	5.09	5.97
Fe I	5202.34	2.18	-1.87	5.18	...
Fe I	5216.28	1.61	-2.08	5.01	...
Fe I	5217.40	3.21	-1.16	5.13	6.10
Fe I	5225.52	0.11	-4.79	...	6.23
Fe I	5242.46	3.63	-0.97	5.06	5.99
Fe I	5243.78	4.26	-1.12	5.27	6.17
Fe I	5247.05	0.09	-4.95	5.11	6.07
Fe I	5250.21	0.12	-4.94	5.06	6.19
Fe I	5266.56	3.00	-0.39	4.98	...
Fe I	5281.80	3.04	-0.83	5.02	5.90
Fe I	5283.63	3.24	-0.52	5.09	6.03
Fe I	5288.52	3.68	-1.51	...	6.15
Fe I	5302.31	3.28	-0.72	5.00	...
Fe I	5307.36	1.61	-2.99	5.03	6.11
Fe I	5322.01	2.28	-2.80	4.99	...
Fe I	5324.19	3.21	-0.10	5.02	5.73
Fe I	5328.04	0.92	-1.47	5.17	5.62
Fe I	5328.54	1.56	-1.85	4.97	5.89
Fe I	5329.99	4.08	-1.22	...	6.09
Fe I	5332.92	1.56	-2.78	4.99	5.96
Fe I	5339.94	3.27	-0.72	5.11	5.91
Fe I	5364.87	4.45	0.23	5.15	5.92
Fe I	5365.40	3.56	-1.02	4.86	...
Fe I	5367.47	4.42	0.44	5.01	5.86
Fe I	5369.97	4.37	0.54	4.97	...
Fe I	5371.50	0.96	-1.64	5.22	...
Fe I	5373.71	4.48	-0.84	...	5.85
Fe I	5383.38	4.31	0.65	4.96	5.79
Fe I	5386.33	4.16	-1.74	...	5.94
Fe I	5393.18	3.24	-0.71	4.97	5.83
Fe I	5397.14	0.92	-1.98	5.19	5.91
Fe I	5398.28	4.45	-0.71	...	5.88
Fe I	5405.77	0.99	-1.84	5.37	5.80
Fe I	5410.91	4.47	0.30	5.10	5.85
Fe I	5415.20	4.39	0.64	4.91	5.74
Fe I	5424.08	4.32	0.52	5.16	...
Fe I	5429.71	0.96	-1.88	5.28	...
Fe I	5434.52	1.01	-2.12	5.12	5.88
Fe I	5445.04	4.39	0.04	5.16	5.96
Fe I	5446.92	0.99	-1.91	5.36	5.79
Fe I	5463.27	4.44	0.07	5.00	5.92
Fe I	5501.46	0.96	-3.05	5.09	...
Fe I	5506.78	0.99	-2.80	5.07	6.03
Fe I	5569.63	3.42	-0.50	4.98	...
Fe I	5572.85	3.40	-0.28	4.97	...
Fe I	5576.10	3.43	-0.90	5.09	...
Fe I	5586.77	3.37	-0.14	5.03	5.75
Fe I	5615.66	3.33	0.05	4.94	...
Fe I	5618.63	4.21	-1.28	...	6.03
Fe I	5638.26	4.22	-0.84	5.12	6.02
Fe I	5641.43	4.26	-1.15	...	6.08
Fe I	5650.70	5.09	-0.96	...	6.33
Fe I	5653.86	4.39	-1.61	...	6.07
Fe I	5655.17	5.07	-0.69	...	6.08
Fe I	5658.81	3.40	-0.84	5.09	5.98
Fe I	5662.52	4.18	-0.57	5.13	6.06
Fe I	5679.02	4.65	-0.90	...	6.27
Fe I	5686.53	4.55	-0.45	...	5.76
Fe I	5701.54	2.56	-2.22	5.03	6.10

Table 2 — *Continued*

Ion	λ (Å)	χ (eV)	$\log gf$	$\log \epsilon$ (X) HD 196944	$\log \epsilon$ (X) HD 201626
Fe II	4491.40	2.86	-2.71	...	5.79
Fe II	4508.29	2.86	-2.44	5.16	5.91
Fe II	4515.34	2.84	-2.60	...	5.77
Fe II	4520.22	2.81	-2.65	5.19	5.95
Fe II	4555.89	2.83	-2.40	5.03	5.86
Fe II	4576.34	2.84	-2.95	5.11	...
Fe II	4582.84	2.84	-3.18	5.07	...
Fe II	4583.84	2.81	-1.93	5.18	5.99
Fe II	4620.52	2.83	-3.21	5.01	...
Fe II	4629.34	2.81	-2.34	5.02	...
Fe II	4656.98	2.89	-3.60	4.92	...
Fe II	4666.76	2.83	-3.28	5.01	6.03
Fe II	4731.45	2.89	-3.10	5.06	5.92
Fe II	4923.93	2.89	-1.26	5.18	...
Fe II	4993.36	2.81	-3.62	4.98	...
Fe II	5018.44	2.89	-1.10	5.25	...
Fe II	5197.58	3.23	-2.22	5.06	5.97
Fe II	5234.62	3.22	-2.18	5.10	5.98
Fe II	5264.81	3.23	-3.13	5.13	...
Fe II	5276.00	3.20	-2.01	5.07	...
Fe II	5284.11	2.89	-3.11	5.04	6.00
Fe II	5316.61	3.15	-1.87	...	6.11
Fe II	5325.55	3.22	-3.16	5.04	5.91
Fe II	5337.73	3.23	-3.72	...	5.92
Fe II	5362.87	3.20	-2.57	5.15	5.99
Fe II	5425.26	3.20	-3.22	5.01	...
Fe II	5432.97	3.27	-3.38	5.21	6.17
Fe II	5534.85	3.25	-2.75	5.05	5.91
Co I	5230.22	1.74	-1.84	...	3.21
Co I	5352.05	3.58	0.06	...	3.33
Co I	5369.58	1.74	-1.65	...	3.56
Co I	5483.35	1.71	-1.41	...	3.40
Co I	6282.63	1.74	-2.17	...	3.79
Ni I	4648.65	3.42	-0.16	3.76	...
Ni I	4756.51	3.48	-0.34	3.77	4.59
Ni I	4829.02	3.54	-0.33	3.79	4.59
Ni I	4831.17	3.61	-0.42	3.98	4.98
Ni I	4904.41	3.54	-0.17	3.84	4.52
Ni I	5017.57	3.54	-0.08	3.87	...
Ni I	5035.37	3.63	0.29	3.72	...
Ni I	5080.53	3.65	0.13	3.96	...
Ni I	5081.11	3.85	0.30	3.83	...
Ni I	5084.09	3.68	0.03	3.77	...
Ni I	5099.94	3.68	-0.28	4.08	...
Ni I	5115.39	3.83	-0.11	3.82	...
Ni I	5146.48	3.71	0.12	3.59	...
Ni I	5476.92	1.83	-0.89	3.82	4.82
Ni I	5754.65	1.94	-2.33	3.84	4.96
Ni I	6108.11	1.68	-2.61	...	4.73
Ni I	6176.82	4.09	-0.53	...	4.87
Ni I	6191.17	1.68	-2.35	...	4.84
Ni I	6586.33	1.95	-2.81	...	4.74
Ni I	6643.64	1.68	-2.01	...	4.63
Ni I	6767.78	1.83	-2.17	...	4.94
Ni I	7555.60	3.85	-0.05	...	5.09
Ni I	7714.31	1.93	-1.97	...	4.73
Ni I	7788.93	1.95	-2.15	...	4.83
Zn I	4722.15	4.03	-0.39	2.43	...
Zn I	4810.53	4.08	-0.17	2.33	...
Y II	4682.32	0.41	-1.51	0.38	...
Y II	4823.31	0.99	-1.12	0.41	...
Y II	4854.87	0.99	-0.38	0.33	1.69
Y II	4883.68	1.08	0.07	...	1.82
Y II	5087.42	1.08	-0.16	0.25	...
Y II	5119.11	0.99	-1.36	0.47	...
Y II	5123.21	0.99	-0.83	0.33	...
Y II	5200.41	0.99	-0.60	...	1.77
Y II	5205.72	1.03	-0.34	0.37	1.79
Y II	5289.82	1.03	-1.85	...	1.68
Y II	5509.90	0.99	-1.01	0.32	...
Y II	5662.93	1.94	0.16	0.51	1.77
Y II	6613.75	1.75	-1.11	...	1.92
Y II	7881.88	1.84	-0.57	...	1.63
Zr I	4466.91	0.63	-1.34	...	3.39
Zr I	5294.82	1.00	-1.49	...	3.60

Table 2 — *Continued*

Ion	λ (Å)	χ (eV)	$\log gf$	$\log \epsilon$ (X) HD 196944	$\log \epsilon$ (X) HD 201626
Zr I	5935.21	0.00	-2.38	...	3.41
Zr I	6049.24	2.46	0.05	...	3.72
Zr I	6140.46	0.52	-1.41	...	3.62
Zr I	6762.41	0.00	-2.66	...	3.59
Zr II	4379.78	1.53	-0.25	...	2.13
Zr II	4457.41	1.18	-1.22	...	2.79
Zr II	4613.95	0.97	-1.54	...	2.36
Zr II	5350.35	1.77	-1.16	...	2.69
Zr II	6114.85	1.67	-1.71	...	2.61
La II	4526.12	0.77	-0.59	...	1.64
La II	4716.44	0.77	-1.21	...	1.49
La II	4748.73	0.93	-0.54	...	1.32
La II	4920.98	0.13	-0.58	0.32	...
La II	4921.79	0.24	-0.45	0.28	...
La II	5122.99	0.32	-0.85	0.22	...
La II	5290.84	0.00	-1.65	...	1.33
La II	5303.53	0.32	-1.35	...	1.57
La II	5482.27	0.00	-2.23	...	1.20
La II	5797.57	0.24	-1.36	...	1.44
La II	5808.31	0.00	-2.34	...	1.42
La II	6390.48	0.32	-1.41	...	1.63
Ce II	4483.89	0.86	0.15	...	2.09
Ce II	4484.82	1.12	-0.33	...	1.74
Ce II	4486.91	0.29	-0.33	...	2.05
Ce II	4515.85	1.06	-0.24	...	1.84
Ce II	4523.08	0.52	-0.08	0.34	...
Ce II	4539.74	0.33	-0.02	0.14	2.32
Ce II	4551.29	0.74	-0.47	...	2.29
Ce II	4560.97	0.68	-0.22	...	1.95
Ce II	4562.37	0.48	0.19	0.31	2.16
Ce II	4572.28	0.68	0.29	0.22	2.03
Ce II	4593.94	0.70	0.07	0.30	...
Ce II	4628.16	0.52	0.20	0.20	...
Ce II	4739.52	0.53	-1.02	...	2.09
Ce II	4747.17	0.32	-1.27	...	2.03
Ce II	4773.96	0.93	-0.33	...	1.73
Ce II	4882.46	1.53	0.29	...	1.68
Ce II	5187.46	1.21	0.08	...	2.04
Ce II	5274.24	1.04	0.08	...	2.01
Ce II	5330.56	0.87	-0.46	...	1.91
Ce II	5512.06	1.01	-0.46	...	2.06
Pr II	5206.54	0.95	-0.06	...	1.03
Pr II	5219.04	0.79	-0.05	...	0.90
Pr II	5259.71	0.63	0.12	...	1.08
Pr II	5292.61	0.65	-0.26	...	0.95
Pr II	5322.76	0.48	-0.32	...	1.38
Nd II	4368.63	0.06	-0.81	...	1.33
Nd II	4446.38	0.20	-0.35	...	1.70
Nd II	4451.98	0.00	-1.10	...	1.99
Nd II	4465.59	0.18	-1.10	...	1.43
Nd II	4485.94	0.38	-1.44	...	1.67
Nd II	4497.26	0.47	-1.38	...	1.67
Nd II	4513.33	0.06	-1.33	...	1.77
Nd II	4556.73	0.18	-1.35	...	1.50
Nd II	4561.17	0.00	-1.65	...	1.77
Nd II	4567.61	0.20	-1.31	...	1.54
Nd II	4594.45	0.20	-1.36	...	1.71
Nd II	4612.46	0.06	-1.82	...	1.81
Nd II	4763.62	0.38	-1.27	...	1.81
Nd II	4786.11	0.18	-1.41	...	1.61
Nd II	4797.15	0.56	-0.69	...	1.49
Nd II	4820.34	0.20	-0.92	...	2.00
Nd II	4825.48	0.18	-0.42	0.01	...
Nd II	4859.03	0.32	-0.44	...	1.82
Nd II	5192.61	1.14	0.27	...	1.84
Nd II	5212.36	0.20	-0.96	...	1.82
Nd II	5249.58	0.97	0.20	...	1.80
Nd II	5255.51	0.20	-0.67	...	2.01
Nd II	5293.16	0.82	0.10	0.04	1.71
Nd II	5306.46	0.86	-0.97	...	1.75
Nd II	5311.45	0.98	-0.42	...	1.76
Nd II	5319.81	0.55	-0.14	0.00	1.90
Nd II	5356.97	1.26	-0.28	...	2.07
Nd II	5431.52	1.12	-0.47	...	2.05
Nd II	5698.92	1.54	-0.67	...	1.59

Table 2 — *Continued*

Ion	λ (Å)	χ (eV)	$\log gf$	$\log \epsilon$ (X) HD 196944	$\log \epsilon$ (X) HD 201626
Nd II	5702.24	0.74	−0.88	...	1.71
Nd II	5740.86	1.16	−0.53	...	1.77
Nd II	5811.57	0.86	−0.86	...	1.73
Sm II	4424.32	0.48	0.14	...	1.17
Sm II	4434.32	0.38	−0.07	...	1.21
Sm II	4467.34	0.66	0.15	...	0.90
Sm II	4472.41	0.18	−0.96	...	0.83
Sm II	4478.65	0.66	−0.36	...	0.85
Sm II	4499.48	0.25	−0.87	...	0.98
Sm II	4511.83	0.18	−0.82	...	1.07
Sm II	4515.09	0.19	−0.87	...	1.20
Sm II	4523.91	0.43	−0.39	...	0.86
Sm II	4591.82	0.18	−1.12	...	1.28
Sm II	4595.29	0.48	−0.50	...	1.28
Sm II	4704.40	0.00	−0.86	...	1.08
Sm II	4815.81	0.18	−0.82	...	0.81
Sm II	4844.21	0.28	−0.89	...	1.17
Sm II	4854.37	0.38	−1.25	...	0.78
Spectral synthesis analysis					
C (CH)	4246.00	7.10	8.40
C (CH)	4313.00	7.10	8.40
N (NH)	3360.00	6.50	6.70
O I	6300.31	0.00	−9.75	...	7.91
Na I	5682.63	2.10	−1.41	...	4.70
Na I	5688.20	2.10	−0.45	...	4.70
K I	7698.96	0.00	−0.18	...	4.50
Zn I	4810.53	4.08	−0.17	...	3.10
Sr I	5238.55	2.26	−0.05	...	2.90
Sr I	5256.90	2.27	+0.23	...	2.50
Sr II	4077.00	0.00	−1.26	1.20	...
Sr II	4215.00	0.00	−1.32	1.30	...
Y II	4682.32	0.41	−1.51	0.15	...
Y II	4854.87	0.99	−0.38	0.10	1.40
Y II	5087.42	1.08	−0.16	0.20	...
Y II	5119.11	0.99	−1.36	0.30	...
Y II	5205.72	1.03	−0.34	0.30	1.40
Ba II	4554.03	0.00	+0.14	1.00	...
Ba II	4934.10	0.00	−0.16	1.00	...
Ba II	5853.68	0.60	−0.91	1.00	2.40
Ba II	6141.71	0.70	−0.03	...	2.40
La II	4920.98	0.13	−0.58	−0.50	...
La II	4921.79	0.24	−0.45	−0.45	...
Ce II	4562.37	0.48	+0.19	0.15	2.20
Ce II	4628.16	0.52	+0.20	0.15	...
Nd II	4069.26	0.06	−0.57	0.00	...
Nd II	5293.16	0.82	+0.10	−0.05	1.90
Nd II	5319.81	0.55	−0.14	−0.10	2.00
Eu II	4129.72	0.00	+0.22	−2.00	...
Eu II	4205.04	0.00	+0.21	−2.00	...
Eu II	6645.10	1.38	+0.17	...	−0.04
Gd II	4438.25	0.66	−0.82	...	1.00
Dy II	3996.69	0.59	+0.26	...	0.80
Pb I	4057.81	1.32	−0.17	1.50	...

Table 3
NUV Abundance Estimates and Upper Limits

Ion	λ (Å)	χ (eV)	$\log gf$	$\log \epsilon$ (X) HD 196944	$\log \epsilon$ (X) HD 201626	Ref.
Equivalent width analysis						
Ti I	2941.99	0.00	−0.14	3.00	...	1
Ti I	2956.13	0.05	+0.12	2.95	...	1
Ti II	2716.25	1.08	−1.48	3.18	...	1
Ti II	2812.02	1.16	−2.32	2.94	...	1
Ti II	2832.18	0.57	−0.85	3.12	...	1
Ti II	2884.10	1.13	−0.23	2.67	...	1
Ti II	2888.93	0.57	−1.36	3.11	...	1
Ti II	2891.06	0.61	−1.14	2.64	...	1
Ti II	3017.18	1.58	−0.30	3.03	...	1
Ti II	3029.73	1.57	−0.35	2.77	...	1
Ti II	3046.68	1.17	−0.81	3.06	...	1

Table 3 — *Continued*

Ion	λ (Å)	χ (eV)	$\log gf$	$\log \epsilon$ (X) HD 196944	$\log \epsilon$ (X) HD 201626	Ref.
Ti II	3056.74	1.16	−0.79	3.11	...	1
Ti II	3058.09	1.18	−0.42	2.96	...	1
Cr I	2726.50	0.94	−0.35	3.74	...	2
Cr I	3015.20	0.96	−0.20	3.08	...	2
Cr I	3021.56	1.03	+0.61	3.44	...	2
Cr I	3053.87	1.03	−0.15	3.14	...	2
Cr II	2751.87	1.52	−0.29	3.13	...	2
Cr II	2757.72	1.51	−0.36	3.26	...	2
Cr II	2766.54	1.55	+0.32	3.14	...	2
Ni I	2313.98	0.28	+0.33	3.69	...	3
Ni I	2317.16	0.17	+0.17	3.73	...	3
Ni I	2321.97	0.11	−1.93	3.95	...	3
Ni I	2421.23	0.17	−1.62	4.11	...	3
Ni I	2821.29	0.03	−1.41	3.88	...	3
Ni I	2834.55	0.17	−2.63	3.93	...	3
Ni I	2943.91	0.03	−1.17	3.73	...	3
Ni I	2984.13	0.00	−1.50	3.71	...	3
Ni I	2992.59	0.03	−1.22	3.45	...	3
Ni I	3012.00	0.42	+0.00	3.79	...	3
Ni I	3037.93	0.03	−0.52	3.72	...	3
Ni I	3050.82	0.03	−0.10	3.61	...	3
Ni I	3054.31	0.11	−0.60	3.48	...	3
Ni I	3064.62	0.11	−1.15	4.10	...	3
Ni II	2297.49	1.32	−0.33	3.48	...	4
Ni II	2316.04	1.04	+0.27	3.27	...	4
Spectral synthesis analysis						
Mn II	2933.05	1.17	−0.10	2.80	3.50	5
Mn II	2949.20	1.17	+0.25	2.80	3.50	5
Cu I	2824.36	1.39	−1.25	2.20	...	6
Ge I	2651.17	0.17	+0.02	0.25	...	7
Ge I	2691.34	0.07	−0.70	0.25	1.90	7
Ge I	3039.07	0.88	+0.07	0.40	...	7
Zr II	2567.64	0.00	−0.17	0.85	<2.70	8
Zr II	2699.60	0.04	−0.66	0.30	<2.10	9
Zr II	2700.14	0.09	−0.08	0.80	...	8
Zr II	2732.72	0.09	−0.49	1.00	<2.60	8
Zr II	2758.81	0.00	−0.56	0.95	2.70	8
Zr II	2915.99	0.47	−0.50	0.90	2.80	8
Zr II	3054.84	1.01	+0.08	0.85	2.80	9
Nb II	2827.07	0.02	−0.82	−0.40	...	10
Nb II	2877.03	0.33	−0.30	−0.50	...	10
Nb II	2950.88	0.51	+0.24	−0.70	...	10
Mo II	2871.51	1.54	+0.06	−0.30	0.80	11
Cd I	2288.02	0.00	+0.15	−0.70	...	12
Lu II	2615.43	0.00	−0.27	−1.90	−0.40	13
Hf II	2641.41	1.04	+0.57	−1.10	...	14
Os II	2282.28	0.00	−0.05	< −0.90	...	15
Pt I	2659.45	0.00	−0.03	−0.78	0.40	16
Pt I	2929.79	0.00	−0.70	< −0.70	...	16
Au I	2675.94	0.00	−0.47	−1.60	<1.50	17
Pb I	2833.05	0.00	−0.50	1.35	3.10	18

References. — (1) Wood et al. (2013); (2) Bergeson & Lawler (1993); (3) Wood et al. (2014a); (4) Fedchak & Lawler (1999); (5) Den Hartog et al. (2011); (6) Kurucz & Bell (1995); (7) Fuhr & Wiese (2009); (8) Ljung et al. (2006); (9) Malcheva et al. (2006); (10) Nilsson & Ivarsson (2008); (11) Sikström et al. (2001); (12) Morton (2000); (13) Roederer et al. (2010); (14) Lawler et al. (2007); (15) Quinet et al. (2006); (16) Den Hartog et al. (2005); (17) Fivet et al. (2006); (18) Biémont et al. (2000), using hfs presented in Appendix C of Roederer et al. (2012).

Table 4
Final Optical LTE Abundance Estimates for HD 196944 and HD 201626

Species	$\log \epsilon_{\odot} (X)$	HD 196944				HD 201626			
		$\log \epsilon (X)$	$[X/Fe]$	σ	N	$\log \epsilon (X)$	$[X/Fe]$	σ	N
C (CH)	8.43	7.10	+1.08 ^a	0.20	2	8.40	+1.48 ^b	0.20	2
N (NH)	7.83	6.50	+1.08	0.25	1	6.70	+0.38	0.30	1
O I	8.69	7.91	+0.73	0.20	1
Na I	6.24	4.65	+0.82	0.01	2	4.75	+0.02	0.10	2
Mg I	7.60	5.55	+0.36	0.07	6	6.36	+0.27	0.08	4
Al I	6.45	6.19	+1.25	0.07	2
Si I	7.51	6.32	+0.32	0.03	27
K I	5.03	4.50	+0.98	0.20	1
Ca I	6.34	4.32	+0.39	0.04	7	5.19	+0.36	0.03	17
Sc II	3.15	0.78	+0.04	0.03	4	1.76	+0.12	0.10	10
Ti I	4.95	2.81	+0.27	0.02	23	3.73	+0.29	0.03	32
Ti II	4.95	2.82	+0.28	0.03	28	3.79	+0.34	0.04	25
V I	3.93	2.43	+0.01	0.05	1
Cr I	5.64	3.16	-0.07	0.04	18	4.12	-0.01	0.04	17
Cr II	5.64	3.35	+0.12	0.05	9	4.08	-0.05	0.06	4
Mn I	5.43	2.99	-0.03	0.23	4	3.55	-0.37	0.08	9
Fe I	7.50	5.09	-2.41 ^c	0.01	87	5.99	-1.51 ^c	0.02	53
Fe II	7.50	5.09	-2.41 ^c	0.02	25	5.96	-1.54 ^c	0.02	66
Co I	4.99	3.46	-0.02	0.10	5
Ni I	6.22	3.83	+0.02	0.03	15	4.79	+0.08	0.04	16
Zn I	4.56	2.43	+0.28	0.05	2	3.10	+0.05	0.20	1
Sr I	2.87	2.70	+1.34	0.14	2
Sr II	2.87	1.25	+0.79	0.15	2
Y II	2.21	0.38	+0.58	0.03	9	1.76	+1.06	0.03	9
Zr I	2.58	3.55	+2.48	0.07	6
Zr II	2.58	2.52	+1.45	0.12	5
Ba II	2.18	1.00	+1.23	0.05	3	2.40	+1.73	0.20	1
La II	1.10	-0.27	+1.04	0.05	3	1.45	+1.86	0.05	9
Ce II	1.58	0.25	+1.08	0.05	6	2.00	+1.93	0.05	17
Pr II	0.72	1.07	+1.86	0.08	5
Nd II	1.42	-0.01	+0.98	0.05	3	1.75	+1.84	0.03	31
Sm II	0.96	1.03	+1.58	0.05	18
Eu II	0.52	-2.00	-0.11	0.10	2	-0.04	+0.95	0.20	1
Gd II	1.07	1.00	+1.44	0.20	1
Dy II	1.10	0.80	+1.21	0.20	1
Pb I	1.75	1.50	+2.16	0.20	1

^a $[C/Fe] > +1.31$ using corrections of [Placco et al. \(2014a\)](#).

^b $[C/Fe] = +1.50$ using corrections of [Placco et al. \(2014a\)](#).

^c $[FeI/H]$ and $[FeII/H]$ values

Table 5
Final NUV LTE Abundance Estimates for HD 196944 and HD 201626

Species	$\log \epsilon_{\odot} (X)$	HD 196944				HD 201626			
		$\log \epsilon (X)$	$[X/Fe]^a$	σ	N	$\log \epsilon (X)$	$[X/Fe]^b$	σ	N
C I	8.43	7.10	+1.08 ^c	0.20	2
O (OH)	8.69	6.60	+0.32	0.30	1
Ti I	4.95	2.98	+0.44	0.04	2
Ti II	4.95	2.96	+0.42	0.19	11
Cr I	5.64	3.35	+0.12	0.31	4
Cr II	5.64	3.17	-0.06	0.07	3
Mn II	5.43	2.80	-0.22	0.15	2	3.50	-0.42	0.20	2
Ni I	6.22	3.78	-0.03	0.20	14
Ni II	6.22	3.38	-0.43	0.15	2
Cu I	4.19	2.20	+0.42	0.20	1
Ge I	3.65	0.30	-0.94	0.15	2	1.90	-0.24	0.20	1
Zr II	2.58	0.89	+0.72	0.07	6	2.77	+1.70	0.04	3
Nb II	1.46	-0.70	+0.25	0.20	1
Mo II	1.88	-0.30	+0.23	0.20	1	0.80	+0.43	0.20	1
Cd I	1.71	-0.70	0.00	0.20	1
Lu II	0.10	-1.90	+0.41	0.20	1	-0.40	+1.01	0.20	1
Hf II	0.85	-1.10	+0.46	0.20	1
Os II	1.40	< -0.90	< +0.11	0.20	1
Pt I	1.62	-0.78	+0.01	0.20	1	0.40	+0.29	0.20	1
Au I	0.92	-1.60	-0.11	0.20	1	<1.50	< +2.09	...	1
Pb I	1.75	1.35	+2.01	0.20	1	3.10	+2.86	0.20	1

^a $[Fe/H] = -2.41$

^b $[Fe/H] = -1.51$

^c $[C/Fe] > +1.31$ using corrections of [Placco et al. \(2014a\)](#).

Table 6
Systematic Abundance Uncertainties

Elem	ΔT_{eff} −150 K	$\Delta \log g$ −0.5 dex	$\Delta \xi$ −0.3 km s ^{−1}	σ_{tot} (dex)
HD 196944				
Fe I	−0.18	−0.01	+0.03	0.18
Fe II	−0.06	−0.19	+0.03	0.20
Na I	−0.17	+0.14	+0.14	0.26
Mg I	−0.16	+0.06	+0.03	0.17
Ca I	−0.12	−0.01	+0.00	0.12
Sc II	−0.14	−0.13	−0.06	0.20
Ti I	−0.24	−0.05	+0.06	0.25
Ti II	−0.13	−0.19	−0.01	0.23
Cr I	−0.12	−0.04	−0.03	0.13
Cr II	−0.03	−0.20	−0.02	0.20
Mn I	−0.19	−0.04	−0.06	0.20
Ni I	−0.16	−0.04	−0.04	0.17
Zn I	−0.14	−0.08	−0.04	0.17
Y II	−0.17	−0.13	−0.05	0.22
Ba II	−0.16	−0.09	+0.19	0.26
La II	−0.19	−0.24	−0.06	0.31
Ce II	−0.19	−0.23	−0.03	0.30
Nd II	−0.22	−0.25	−0.08	0.34
HD 201626				
C I	+0.11	−0.19	+0.00	0.22
O I	+0.15	−0.18	+0.01	0.23
Mg I	−0.15	+0.06	+0.05	0.17
Fe I	−0.17	+0.06	+0.08	0.20
Fe II	+0.01	−0.18	+0.10	0.21
Na I	−0.09	+0.01	+0.01	0.09
Al I	−0.05	+0.01	+0.01	0.05
Si I	−0.04	−0.01	+0.01	0.04
K I	−0.19	+0.11	+0.10	0.24
Ca I	−0.14	+0.06	+0.07	0.17
Sc II	−0.04	−0.18	+0.06	0.19
Ti I	−0.18	+0.02	+0.05	0.19
Ti II	−0.03	−0.17	+0.08	0.19
Cr I	−0.18	+0.03	+0.08	0.20
Cr II	+0.02	−0.19	+0.02	0.19
Mn I	−0.17	+0.01	+0.03	0.17
Co I	−0.17	+0.00	+0.06	0.18
Ni I	−0.16	+0.01	+0.06	0.17
Y I	−0.06	−0.17	+0.16	0.24
Zr I	−0.19	+0.02	+0.01	0.19
Zr II	−0.05	−0.19	+0.10	0.22
La II	−0.08	−0.18	+0.14	0.24
Ce II	−0.08	−0.17	+0.20	0.27
Pr II	−0.08	−0.18	+0.11	0.23
Nd II	−0.11	−0.18	+0.15	0.26
Sm II	−0.08	−0.18	+0.16	0.25